FEASIBILITY OF MINIMALLY INVASIVE FIBER BASED EVALUATION OF CHONDRODYSTROPHOID CANINE INTERVERTEBRAL DISC BY REFLECTANCE SPECTROSCOPY

By

YUANYUAN JIANG

Master of Science in Precision Instrument and

Opto-Electronics Engineering

Tianjin University

Tianjin, China

2008

Submitted to the Faculty of the
Graduate College of the
Oklahoma State University
in partial fulfillment of
the requirements for
the Degree of
MASTER OF SCIENCE
May 2011

FEASIBILITY OF MINIMALLY INVASIVE FIBER BASED EVALUATION OF CHONDRODYSTROPHOID CANINE INTERVERTEBRAL DISC BY REFLECTANCE SPECTROSCOPY

Thesis Approved:

Dr. Daqing Piao

Thesis Adviser

Dr. Kenneth E. Bartels

Dr. Charles F. Bunting

Dr. Mark E. Payton

Dean of the Graduate College

ACKNOWLEDGMENTS

First, I would like to offer my sincerest gratitude to my advisor, Dr. Daqing Piao, for his support and guidance on this project, for his patience, motivation, enthusiasm, and knowledge. This thesis would not have been possible without all the inputs from Dr. Piao.

I am eternally grateful for my committee, Dr. Kenneth E. Bartels for letting me experience the research on canine intervertebral disc, patiently correcting my writing and financially supporting my research, and Dr. Charles F. Bunting for his kind encouragement and insightful comments.

I also particularly thank Dr. Kelci McKeirnan in Department of Veterinary Clinical Sciences for her great clinical collaboration. Without all the samples she collected and prepared, the *in situ* cadaveric operations, and so on, this work could not have been done.

Great thanks to my lab mates, Zhen Jiang, Guan Xu, Anqi Zhang and Wei Sun for all the discussions and helps on this thesis. Also thanks to my friends, for making my life easier and happier.

Last but not least, I would like to thank my family. I thank my parents, Zumao Jiang and Shujun Wang. It was their supporting, understanding and love that makes this work possible. I thank my husband, Yongli Qi, who gives me love and support. It is he who gives me encourage in times of difficulties and shares joy with me in times of happiness. I also thank my oncoming son, who brings me the joy, hope and faith during the completion of this work.

This work is made possible by funding from Kerr Foundation, Oklahoma City, OK to Dr. Bartels.

TABLE OF CONTENTS

Chapter Page

LIST OF TABLES

Table Page

LIST OF FIGURES

Figure Page

Figure Page

CHAPTER I

INTRODUCTION

1.1 Overview

This thesis proposed to use a broad band single fiber reflectance spectroscopy system to evaluate the mineralization of the canine intervertebral disc. The canine intervertebral discs, especially chondrodystrophoid discs are susceptible to intervertebral disc degeneration, which involves water dehydration and calcification within the nucleus pulposus. By placing a single fiber via spinal needle into nucleus pulposus within canine intervertebral disc, the optical properties of the nucleus pulposus would be derived according to its reflectance spectrum. The calcification within the degenerated discs should increase light scattering and the loss of water is expected to reduce light absorption.

In this thesis, the configuration of single fiber reflectance spectroscopy system is introduced, the system is evaluated and its reflectance spectrum is calibrated. The reflectance spectra of both Intralipid and cadaveric discs are analyzed. The model for single fiber reflectance spectroscopy is validated by Intralipid phantom study. And the spectrum differences between pre and post ablation discs and between normal and calcified discs are compared and analyzed.

The thesis is organized into six chapters:

Chapter 1: Introduction

Chapter 2: Background

Chapter 3: Instrumentation

Chapter 4: Phantom studies

Chapter 5: Cadaver studies

Chapter 6: Conclusion and discussion

1.2 Motivation

Intervertebral disc degeneration is a common and painful disease that occurs in dogs, especially chondrodystrophoid breeds. Intervertebral disc degeneration involves water dehydration and calcification within the nucleus pulposus, which will degrade the “shock absorber” function of intervertebral disc. With time, disc herniation potentially develops, which means the nuclear material will herniation through the annulus wall and compress the spinal cord. Disc herniation could cause intense lumbar pain and even paralysis in dogs, and has to be treated immediately. To prevent the recurrence of disc herniation, percutaneous laser disc ablation (PLDA) is recommended [1]. Clinically, radiography is used to assess the disc condition prior to PLDA, and calcification within the nucleus pulposus appears as an opacity on radiographs [2]. However, not all degenerated discs will be calcified and some partially calcified discs cannot be observed by radiography. Consequently, the sensitivity of radiography is low. In addition, the output of PLDA is difficult to be evaluated in-line. Therefore, developing an intervertebral disc evaluation system that could be used in conjunction with the PLDA procedure is ideal.

In this study, a single fiber based broad band reflectance spectroscopy system was developed to evaluate the intervertebral disc conditions before and after the PLDA procedure. The single fiber

configuration makes the operation compatible with the unique narrow disc spaces and small anatomical structure of the nucleus pulposus through needle insertion. And it can also be implemented for use with the PLDA procedure. The optical properties derived from the reflectance spectrum, reflecting both morphological and biochemical changes due to the degeneration, could be used to alter the PLDA procedure to improve efficacy.

1.3 Related studies

Intensive studies have been done on using optical techniques to identify changes that occur in biological tissues associated with disease progression *in vivo*. In terms of intervertebral disc, there have been several studies on using optical method to diagnose intervertebral disc degeneration. Recent studies show the possibility of using polarization-sensitive optical coherence tomography to diagnose degenerated intervertebral discs in bovine and equine species [2, 3]. Because of the lamellar structure of annulus fibrosus, optical coherence tomography could detect the structure of the annulus fibrosus layers. Structural changes of the outer annulus fibrosus due to disc herniation could be visulized on optical coherence tomography. Using optical coherence tomography, the contrast between normal and degenerated disc comes from structural alterations, specifically discontinuity, of the outer annulus fibrosus. However, for chondrodystrophoid dogs, the annulus fibrosus does not illustrate apparent discontinuity until a very late stage. Since the structrual alteration may be preceeded by bio-chemical changes, sensitivity to the tissue microscopic constituents may render earlier and more accurate diagnosis of intervertebral disc degeneration.

Reflectance spectroscopy is a method that is capable of noninvasively or minimally invasively determining tissue scattering and absorption properties, which are related to tissue's micro-architecture and bio-chemical compositions. This information can be used to describe tissue physiology, such as vascular oxygen saturation, blood volume, and cellular morphology, such as cell or organelle size and density [4-6]. Intensive studies have been performed using reflectance spectrum to diagnose diseases in various organs [7-9]. However, the majority of reflectance

spectroscopy systems utilize multiple optical fibers to deliver and collect light during measurements, and the distance between the source and detector must be far enough for applying the theory of diffuse scattering[10, 11]. Diffuse reflectance spectroscopy detects changes from larger area and allows the light to penetrate deeper into the tissue, which is desired for some application, such as imaging breast or prostate [12, 13]. However, for other applications, a smaller source detector separation or even single fiber configuration is desired. Smaller source detector separation results in smaller probe size and usually simpler device design, making it more suitable for some medical uses, such as optical biopsy via endoscopy [14]. Reflectance signal results from elastic scattering within small local medium when the source and detector are located in close approximation. Other studies have shown the potential of distinguishing cancerous and noncancerous tissues by measuring the elastic scatter or fluorescence [15, 16]. For this study, single fiber configuration is preferable because a small diameter fiber accommodates the small narrow anatomically structure of nucleus pulposus in a canine intervertebral disc.

Previous studies have been performed on reflectance spectroscopy with a single fiber configuration. The photon path length and sampling depth of single fiber reflectance has been simulated by Monte Carlo Simulation and validated by phantom tests [14, 17]. The potential for staging lung cancer using the single fiber reflectance spectroscopy has also been demonstrated [18].

For most studies, the primary absorber within the tissue is hemoglobin. As shown in Fig. 1.1, the absorption coefficients of water and hemoglobin are relatively low in Near Infrared (NIR) band compared to that in visible or longer wavelength band. Therefore, the use of infrared light offers advantages over visible light in that it can sample deeper regions of tissue, has better penetration of the denser skull in brain studies, and is less sensitive to blood vessel artifacts [19]. However, one of the main differences of this study from other studies is that the intervertebral disc tissue is relatively avascular and the main light absorber is water. Considering this fact, the absorption

spectrum could extend to the visible light range, where the hemoglobin has high absorption but the water absorption is relatively low.

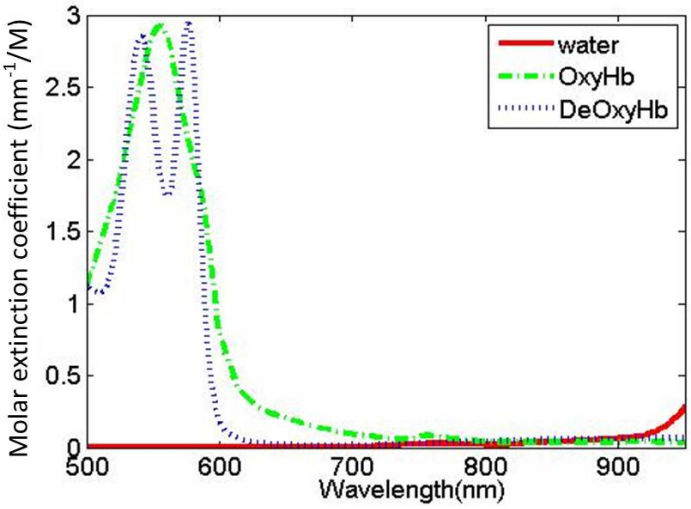

Fig. 1.1 Absorption spectrum of water and hemoglobin. (Data from references [20, 21])

This study was proposed based on the following hypotheses: (1) degenerative intervertebral discs will likely have increased optical scattering as a result of calcification; (2) degenerated intervertebral discs will be associated with a decrease in optical absorption due to water loss, specifically at the spectral peaks sensitive to water content. Both mechanisms are expected to contribute to increasing the spectral reflectance intensity in a single-fiber configuration.

The current work involves primarily the construction of a single-fiber based reflectance spectrsocpy system and calibration of the system. Preliminary analysis of the data acquired from cadeveric canine intervertebral discs prior to and after PLDA, and from normal and calcified cadeveric discs demonstrated that the changes of diffuse reflectance spectra ranging from 500 nm to 950 nm correlate with the expected changes in optical scattering within the intervertebral disc.

CHAPTER II

BACKGROUND

2.1 Background of canine intervertebral disc and intervertebral disc degeneration

Canine intervertebral disc lies between the vetebrae and acts as a soft cushion between the vetebrae. Intevertebral disc disease is a common, frequently debilitating, painful and sometimes fatal neurologic disease that occurs in dogs. A similar condition of intervertebral disc degeneration with extrusion/protrusion is also a relatively common neurologic condition in human patients. In this section, I will introduce some background on canine intervertebral discs and disc disease.

2.1.1 Introduction to Canine intervertebral disc

2.1.1.1 Anatomy of canine intervertebral disc

Canine intervertebral discs are located between each pair of vertebrae along almost the entire length of the canine spinal column. The canine spinal column is made up of four major vertebral regions: cervical (neck), thoracic (chest), lumbar (back) and sacral (pelvic). Dogs have seven cervical, thirteen thoracic, seven lumbar and three sacral vertebrae, as shown in Fig.2.1 [22]. Intervertebral discs are located between the vertebral bodies starting from the second and third cervical vertebrae (C2-3) and extending to the seventh lumbar and first sacral vertebrae (L7-S1).

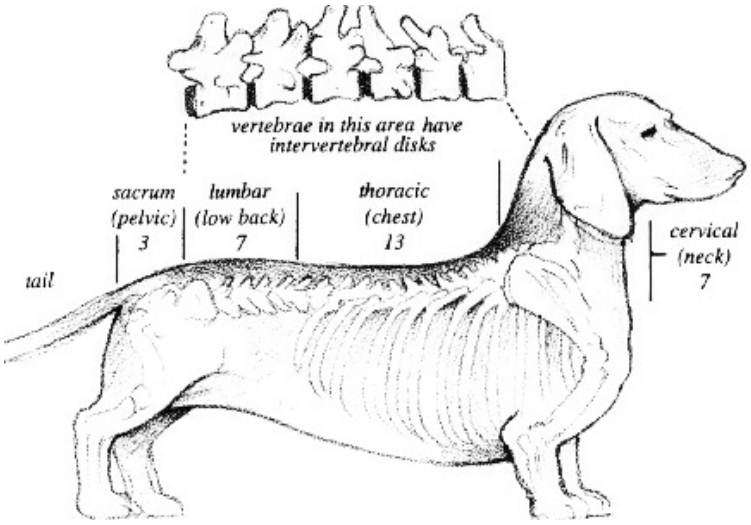

Fig. 2.1 Anatomy of canine intervetebral disc

Intervertebral disks are composed of two major anatomic zones: annulus fibrosus and nucleus pulposus, as shown in Fig.2.2.

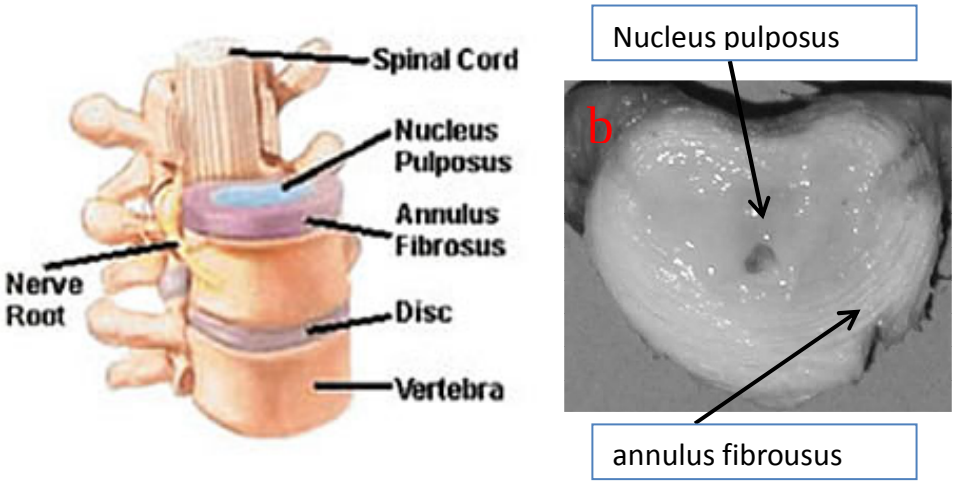

(a) Schematic of the intervertebral disc structure [23] (b) Photo of intervertebral disc [24]

Fig. 2.2 Intervertebral disc antatomical structure

The annulus fibrosus is a fibrous basket that envelops the nucleus pulposus [25]. In transverse section, it appears as concentric rings of fibrous tissue which completely encircle the nucleus pulposus [26]. It has been shown that the lamellar layers are interrupted most frequently at the

dorsolateral aspect of the annulus fibrosus. At that level of lamellar discontinuity may induce an inherent weakness at this point [27].

The nucleus pulposus is a gelatinous inner core. The principal component of the nucleus pulposus is water, making up to 80% to 88% of its content [26]. Water is confined to the disc in the form of proteoglycan, making the nucleus mostly transparent and appearing as a viscoelastic gel [28]. When sectioned, moisture will persistently extrude from nucleus pulposus [29].

2.1.1.2 Functions of canine intervertebral disc

The canine intervertebral discs play the role of elastic cushions between the vertebrae. They allow movement, minimize trauma and shock, and help connect the spinal column. The spinal column supports the attachment of muscles and bones and also protects the delicate nervous system while maintaining flexibility for movement. Intervertebral discs acts as a deformable tissue between the individual vertebral bodies in order to enable mobility of the vertebral column. This role requires it to be flexible enough to permit the extremes of movement associated with local motion, yet rigid enough to withstand the normal physiological forces acting along the vertebral column.

Intervertebral discs are designed well to dispose of compressive forces [22]. When a disc is compressed, both nucleus pulposus and annulus fibrosus share in bearing the load. And when compressive forces are applied, the force is mostly absorbed by the gelatinous nucleus pulposus and the nucleus tries to deform by spreading radially [30]. As the nucleus pulposus is squeezed, the annulus fibrosus with its unique layers of fibers reacts by sliding over each other to form a more tightly packed arrangement to prevent that expansion, as shown in Fig. 2.3. The annulus effectively "braces" from within thus preventing buckling [22].

However, intervertebral discs are not as well designed to combat twisting applied to the axis [31]. When twisting forces are applied, only half of the annular fibers are approximately oriented to resist this rotation and the other half are shortened or become slack and therefore can’t help

prevent the movement. In this process, the nucleus pulposus plays a smaller role as a "ball bearing". Consequently, there is more possibility for a tearing injury of the annular fibers [22]. With time, repetitive twisting forces may significantly weaken the annulus fibrosus and prevent its ability to resist compressive forces as efficiently.

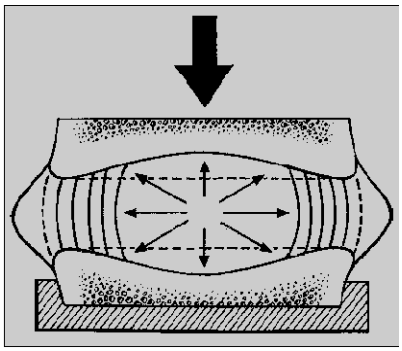

Fig. 2.3 The response of intervertebral disc to compressive force [26]

A degenerating nucleus pulposus can have serious consequences on the function of intervertebral disc and vertebral column. The changes that occur in the degenerated intervertebral disc and particularly in the nucleus pulposus will be introduced in following sections.

2.1.2 Introduction to canine intervertebral disc diseases

2.1.2.1 Two types of canine intervertebral discs and disc herniation

There are two types of canine breeds based on the type of degeneration occurs in the nucleus pulposus: chondrodystrophoid and nonchondrodystrophoid. The word “chondrodystrophoid” literally means faulty development or nutrition of cartilage. In humans, the word “chondrodystrophoid” means physically dwarfism. In dogs, chondrodystrophoid breeds refer to the breeds of dogs that have disproportionately short and angulated limbs, such as Dachshund, Bulldog, and Bassett hound.

There are significant differences between disc degeneration in the nonchondrodystrophoid and chondrodystrophoid breeds [32]. For nonchondrodystrophoid discs, disc degeneration is typically confined to one single disc with little chance of calcification in the nucleus pulposus. However,

for chondrodystrophoid discs, disc degeneration potentially occurs simultaneously in all the discs along the entire length of the vertebral column. In addition, nonchondrodystrophoid disc degeneration typically is associated with old age while degeneration in chondrodystrophoid discs could occur in relative young dogs. Furthermore, chondrodystrophoid disc degeneration is often associated with the explosive herniation of degenerated nuclear material from the annulus fibrosus, which could cause serious pain and paralysis.

Disc degeneration can lead to herniation. Hansen classified the intervertebral disc herniation into two types [28]: type I herniation and type II herniation, as shown in Fig. 2.4. Type I herniation refers to an acute and profound herniation. It involves the degeneration of the annulus fibrosus and mineralization of the nucleus pulposus. The herniation usually occurs in the dorsal direction and the outer annulus is ruptured acutely, allowing a large amount of nuclear core to escape. The calcified nucleus pulposus materials press against the spinal cord and cause serious pain and neural destruction. Type I herniation usually occurs in the chondrodystrophic breeds, although it could also be a problem to nonchondrodystrophic breeds if extreme physical activity or trauma is applied. Type II herniation is usually a slower, more gradual process and only a small amount of nucleus pulposus will herniate. In type II herniation, the nucleus pulposus usually penetrates to the annulus area resulting in protrusion instead of actual herniation. Type II herniation is more common in nonchondrodystrophic discs.

When chondrodystrophoid disc degeneration occurs, it tends to be more serious and often be catastrophic, i.e., paralysis. In this paper, we focus on the chondrodystrophoid disc degeneration.

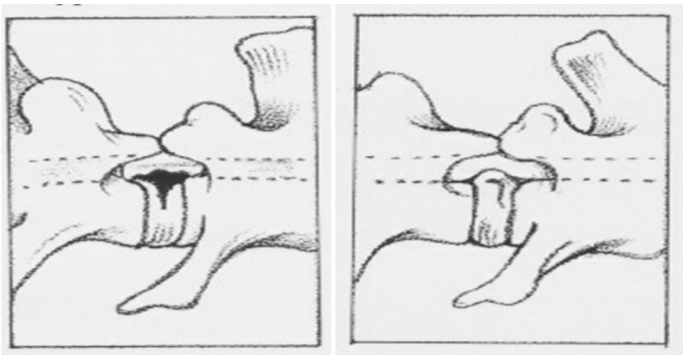

(a)Type I herniation (b) Type II herniation

Fig. 2.4 Two types of herniations [22]

2.1.2.2 Chondrodystrophoid disc degeneration and herniation

For chondrodystrophoid discs, degeneration can occur in dogs at relatively early age simultaneously along the entire spinal column. The intervertebral disc of a newborn chondrodystrophoid puppy is transparent, similar to nonchondrodystrophoid disc. However, the biochemical analysis shows there are lower proteoglycan concentration and higher collagen concentration in chondrodystrophoid than in nonchondrodystrophoid discs, which means chondrodystrophoid breeds may lack the hydraulic properties from birth [32]. Consequently, the degeneration occurs rapidly in chondrodystrophoid discs. Nucleus pulposus begins to dehydrate in dog as young as two month old. Dehydration makes the nucleus lose its elasticity and diminishes its shock absorber roles. Eventually calcification will occur, which makes the nucleus pulposus even less elastic. By the age of one year, the viscoelastic gel nucleus appears to be grayish white or grayish yellow in color and the change occurs in the entire spinal column almost simultaneously. Partial or complete calcification of the nucleus will occur in single disc or along the entire vertebral column. Calcification has been reported in dogs as young as five months of age [32]. Postmortem examination revealed that for dogs over two years old, 60% to 70% of intervertebral discs have been calcified. Changes in the nucleus results in alternations in its biomechanical properties, which will place more of the “workload” onto the annulus fibrosus. As

more pressures are applied, the hardened nucleus pulposus will eventually break through the weakened annulus wall, especially at its weakest point, the thinner dorsal area lying just below the spinal canal, and compress the spinal cord. Consequently, the mass compression to the spinal cord may cause serious pain and severe neurological problems in dogs.

2.1.3 Diagnosis and treatment of canine intervertebral disc degeneration

2.1.3.1 Diagnosis of canine intervertebral disc degeneration

Intervertebral disc herniation is usually suspected when the dog shows signs of back pain. Spinal radiographs will be taken to aid in diagnosis. General anesthetic needs to be administered during spinal radiographs because the movement or the tension of muscles will obscure the image. Once the dog is anesthetized, a series of radiographs will be taken in both lateral and ventral sides[22]. Calcification in the nucleus will appear opaque on the radiographic image, which is often a sign of disc degeneration. Although calcification does not necessary mean the disc will herniate and cause serious problems, the chances are increased due to the poor elasticity of the nucleus pulposus caused by calcification. However, not all degenerated discs will be significantly calcified to be evident in radiographs. Radiography is reported to have a sensitivity of 60% and specificity of 100% when using histopathology as the gold standard [2].

For more accurate diagnosis, myelographic examination could be performed. During myelogram, radiopaque dye is injected into the cerebrospinal fluid in the subarachnoid space [22]. For normal discs, two columns of dye will run in parallel to each other on both sides of the spinal cord. When herniation occurs, the normal parallel dye column will appear compressed or expanded due to the eruption of the nuclear material. Using a myelogram, disc herniation can be localized and degree of the herniation and the side of herniation can be determined.

Low-field magnetic resonance imaging (MRI) can also be used to evaluate intervertebral disc degeneration in dogs. MRI has a specificity of 79% and sensitivity of 100% compared to

histopathology [33]. However, MRI is much more expensive than radiography and MRI machines for veterinary use is limited. At this point for most practices, radiographic examination is still most suitable and used method for diagnosis of canine intervertebral disc degeneration.

2.1.3.2 Treatment of canine intervertebral disc degeneration

Canine intervertebral disease should be treated as soon as it has been diagnosed. For mild cases, anti-inflammatory and pain medicine treatment is prescribed along with an extreme excise restriction. For more severe cases, surgery, such as decompressive hemilaminectomy or dorsal laminectomy, is needed to remove the herniated disc material that is compressing the spinal cord. The spinal cord undergoes irreversible damage if injury occurs and is not decompressed in time. The spinal cord is very sensitive to the oxygen and glucose supply. If vascularity is compressed by the herniated disc nucleus material, the spinal cord starts to undergo myelomalacia. The degree of the damage depends on the time the spinal cord goes without proper oxygen and glucose supply. For type I disc herniation, the herniated nuclear material compresses the spinal cord with a great force within a short period of time, which may cause serious problems. Therefore, prophylactic surgery may be recommended to the susceptible discs, especially those in chondrodystrophoid dogs.

A recommended prophylactic procedure for reducing the risk of disc hernaiton recurrence in dogs is percutaneous laser disc ablation (PLDA), a minimally invasive procedure that uses a holmium yttrium aluminum garnet (Ho:YAG) laser to ablate the nucleus material in intervertebral discs [1]. PLDA is reported to reduce the volume and stabilize the nucleus pulposus, thereby reducing the risk of neurologic recurrence to approximately 3.4% [1].

2.1.3.3 Preventative proceduere --- PLDA

Percutaneous laser disc ablation was developed by Dr. Kenneth E. Bartels at Oklahoma State University (OSU). PLDA is a preventative procedure to reduce the disc herniation that is

recommended for dogs with a prior history of disc disease or dogs having righ risk of disc herniation [34]. PLDA is not a procedure that could replace the decompressive surgery treatment to dogs that are paralyzed or have acute thoracolumbar pain. It is aimed to reduce the recurrence rate of disc diseases.

PLDA is a minimally invasive precedure that uses Holmium yttrium aluminum garnet (Ho:YAG) laser to vaporize the canine discs' nucleus pulposus. Candidates for PLDA are dogs that have recovered from previous surgical or medical treatment and are currently neurologically normal. Before ablation, the dog is anesthetized and place on its side, as shown in Fig. 2.5. Twenty gauge myelographic needles are placed perctaneously throught the annulus into the center of discs (usually between T10 and L4) guided by radiography to identify the correct position, shown in Fig. 2.6. The laser fiber is then introduced ito the discs' nucleus pulposus through the needles. Ho:YAG laser is then actived to vaporiaze and congulate the nuclear material. This process diminishes and presumable stabilizes the nucleus, which helps eliminate the chance of disc herniation.

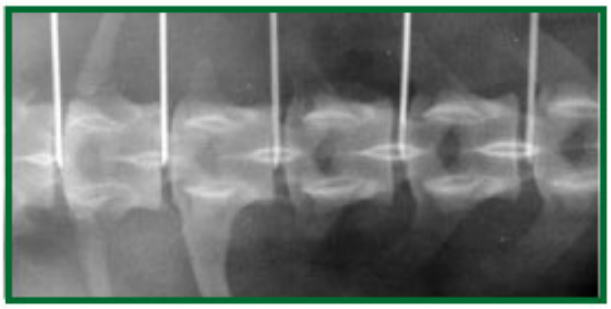

Fig. 2.5 Dog undergoes PLDA [34] Fig. 2.6 Using radiography to locate needle position [35]

Although PLDA is widely used at OSU and by other veterinarians, performing PLDA on susceptible dogs is still not a prevalent procedure. Part of the reason is the inability to accurately evaluate the pre and post ablation disc condition. Although radiographic images are taken to assess the pre-ablation disc condition, radiography has a sensitivity of only 60% [2]. In addition,

due to the lack of post-ablation evaluation method, laser-tissue interaction involving degenerative intervertebral discs, especially calcified discs, couldn't guarantee total ablation of the nucleus. Therefore it is ideal to develop an imaging or sensing method for PLDA evaluation, preferable to be used in conjunction with PLDA.

In this study, we developed a single fiber-needle based reflectance spectroscopy system for pre and post ablation intervertebral disc assessment during PLDA procedure. The principle and configuration of the fiber needle reflectance spectroscopy system will be discussed in following chapters.

2.2 Introduction to reflectance spectroscopy

Reflectance spectroscopy is extensively employed for noninvasive or minimally invasive qualification or quantification of tissue optical properties [36, 37], which are determined by tissue micro-architecture and bio-chemical compositions. Tissues can be characterized by their optical properties, such as the absorption coefficients (μ_a), the scattering coefficient (μ_s), the phase function ($p(\theta)$), the anisotropy value ($g =< \cos(\theta) >$) and the reduced scattering coefficient ($\mu_s' = u_s(1-g)$). Correlation of these optical properties with tissue's histological and biochemical characteristics provides a wealth of information regarding tissue's composition and biochemistry. Such information is very useful for the study of tissue morphology and physiology. Early detection and diagnosis of cancer [18, 38-40] and blood flow assessment [41, 42] could also be obtained from these information.

There have been intensive study on the biomedical applications of reflectance spectroscopy. The absorption coefficients obtained from reflectance spectroscopy contains the biochemcial information of the tissue. A wide variaty of biological tissue chromophores have been quantitatively assessed by way of measuring of absorption coefficient, such as hemoglobin in its oxygenated and deoxygenated forms[43, 44], melanin [7], bilirubin [45] and cytochromes [8, 46],

etc. On the other hand, the scattering properties derived from reflectance spectroscopy convey the morphological charateristics of the biological tissues and could be related with the size and density of sub-cellular organelle [47, 48]. Furthermore, physilogical process and charcteristics, such as microcirculation [44, 49, 50], hemodynamics [51], erythema [52] and metabolism [46] may also be monitored using reflectance spectroscopy. Reflectance spectroscopy has shown potential in diagnosing cancers or some precancerous lesions in various organs, such as colon [43, 53], esophagus [54], stomach [49], bladder [9, 15], cervix [55, 56], ovaries [57], breast [58, 59], brain [60], liver [8], pancreas [50], heart [61], oral tissue [62] and skin [7, 63] etc.

Many configurations of reflectance spectroscopy are based upon diffuse reflectance measurement. Diffusion approximation [59, 64, 65] is widely used for modeling light propagation in biological tissue. However, diffusion approximation is applies to two conditions: one is that the medium is scattering dominant, which means that the medium has much higher scattering than absorption, or $\mu_s' \gg \mu_a$; the other is that there is large separation between source and detector, or $\rho \gg {}^{1}/_{\mu_s'}$. The scattering dominant medium condition is satisfied in biological tissues for 500-950nm. However, the large source detector separation condition is not necessary satisfied for all reflectance spectroscopy configurations.

Diffuse reflectance measurements employ multiple source detector fibers, have long source-collector fiber optical distances, and could sample large volumes. The large volume measurements of optical properties are desired in many applications, such as measurements in breast, prostate and other tissues. However, in some clinical cases, localized measurements are required, especially for operation during an interstitial procedure, in surgical field or in small anatomical structures. Spatially-constrained reflectance spectroscopy has been developed with small source collector fiber separation to address this need [66]. The source fiber delivers broadband light and the reflectance spectrum is detected by collector fiber located at a distance, *r*, which could be very small, from the source. A number of studies have been performed using a

small source detector pair separation configuration , specifically for liver cancer diagnosis [40]. As an important parameter that influences the reconstruction of optical properties in a small source detector separation system, the separation distance between the source and detector fibers has been under intensive investigations [67, 68]. Furthermore, single fiber configuration has been developed in order to fit the reflectance spectroscopy system for needle biopsy, and small volumes of tissue [14, 17, 18]. Unlike other fiber optic reflectance systems that utilize multiple optical fibers to deliver and collect light during measurement, single fiber reflectance configuration utilizes one fiber as both source and detector, which could be easily fitted into spinal needle or biopsy channel of interventional device. A single fiber reflectance spectroscopy system detects localized optical properties and offers the advantages of having a small probe profile and a compact detection device. For this study, the unique small and narrow anatomical structure of intervertebral disc's nucleus pulposus makes single-fiber probe configuration a natural choice.

For reflectance spectroscopy with a small source detector separation or single fiber, diffusion approximation is not accurate for describing the light propagation within the medium. For small fiber and detector separation, the reflectance comes from single or elastic scattering. Non-diffuse reflectance spectroscopy measures only a small volume of tissue, which is typically less than 1 mm^3 [4]. According to studies done on elastic scattering reflectance spectroscopy, the reflectance spectrum R has linear relationship with the reduced scattering coefficient of the medium if the absorption is negligible [69],

$$R = a\mu_s' + b \tag{2.1}$$

where a and b are some constant numbers.

When considering the absorption of the medium, the absorption by the tissue could be modeled using Lambert-Beer's Law and the reflectance spectrum R is modeled as the product of scattering spectrum and absorption spectrum[10].

$$R = (a\mu_s' + b)e^{-u_a L} \tag{2.2}$$

where L is the optical path length of the light from leaving the fiber tip to returning to the fiber tip. Studies show that the path length is a function of both the absorption and reduced scattering coefficients. For small source detector separation in two fiber configuration, the optical path length was modeled by [10] as inversely proportional to both scattering and absorption properties of the medium, $L = \frac{b}{(\mu_a \mu_s')^c}$, where b and c are constants. However, for single fiber configuration, S.C. Kanick et al [14, 17] proposed an empirical model for the optical path length, which was validated by both Monte Carlo simulation and phantom experiments. The path length was modeled as $L = \frac{c_1 d e^{c_2 d}}{(u_s' d)^{c_3}(c_4 + (u_a d)^{c_4})}$, where d is the diameter of the fiber and c_1, c_2, c_3, c_4 are constants.

In this study, we modeled the reflectance spectrum as $R = a\mu_s' e^{-u_a L}$ with the path length L being modeled following S.C. Kanick's work.

2.3 Introduction to Mie scattering theory

Scattering is one of the most important optical properties of an object when interacting with radiation. In biological tissue, scattering is expected to occur from cells, organelles and proteins etc. Therefore the scattering properties represent the micro architecture of the tissue. The scattering of light could be explained by electromagnetic wave theory and solved using Maxwell equation. The Mie theory is an analytical solution of Maxwell equation for scattering of electromagnetic radiation by spherical particles whose sizes are not significantly different from the wavelength of the interacting radiation.

2.3.1 Mie scattering theory

For sphere particle of radius *r*, the scattering efficiency Q_{sca} (mm^{-1}) and the scattering anisotropy factor *g*, are defined as [70]

$$Q_{sca} = \frac{2}{x^2}\sum_{l=0}^{\infty}(2l+1)(|a_l|^2 + |b_l|^2) \tag{2.3}$$

$$g = \frac{2}{Q_{sca}x^2}\sum_{l=0}^{\infty}\left[\frac{l(l+2)}{l+1}\mathrm{Re}(a_l a^*_{l+1} + b_l b^*_{l+1}) + \frac{2l+1}{l(l+1)}\mathrm{Re}(a_l b^*_l)\right] \tag{2.4}$$

where $x = kr = \frac{2\pi n_b}{\lambda}r$, and n_b is the refractive index of the background medium. The coefficients a_l and b_l are given by,

$$a_l = \frac{\psi'_l(y)\psi_l(x) - n_{rel}\psi_l(y)\psi'_l(x)}{\psi'_l(y)\zeta_l(x) - n_{rel}\psi_l(y)\zeta'_l(x)} \tag{2.5}$$

$$b_l = \frac{n_{rel}\psi'_l(y)\psi_l(x) - \psi_l(y)\psi'_l(x)}{n_{rel}\psi'_l(y)\zeta_l(x) - \psi_l(y)\zeta'_l(x)} \tag{2.6}$$

where n_{rel} is the relative refractive index coefficient, $n_{rel} = n_s / n_b$, with n_s being the refractive index coefficient of scatter, and $y = n_{rel}x = \frac{2\pi n_s r}{\lambda}$.

$\Psi(),\zeta()$ are Riccati-Bassel functions and $\Psi'(),\zeta'()$ donate the first order derivative. The Riccati-Bassel functions are defined by

$$\psi_l(z) = zj_l(z) = (\frac{\pi z}{2})^{1/2} J_{l+1/2}(z) \tag{2.7}$$

$$\chi_l(z) = -zy_l(z) = -(\frac{\pi z}{2})^{1/2} Y_{l+1/2}(z) \tag{2.8}$$

$$\zeta_l(z) = \psi_l(z) + i\chi_l(z) = zh_l^{(2)}(z) = (\frac{\pi z}{2})^{1/2} H^{(2)}_{l+1/2}(z) \tag{2.9}$$

where *l* and *l*+ ½ are the orders; $j_l()$ *and* $y_l()$ represent the spherical Bassel functions of the first and second kind, respectively; $J_l()$ *and* $Y_l()$ denote the Bessel functions of the first and second

kind, respectively; $h_l^{(2)}()$ is the spherical Hankel function of the second kind; $H_l^{(2)}()$ means the Hankel function of the second kind. Note,

$$h_l^{(2)}() = j_l() - iy_l() \tag{2.10}$$

$$H_l^{(2)}() = J_l() - iY_l() \tag{2.11}$$

The refractive index coefficients of background and scatters are wavelength dependent and could be expressed using Cauchy equations [71],

$$n(\lambda) = A + \frac{B}{\lambda} + \frac{C}{\lambda^2} \tag{2.12}$$

where *A, B, C* are constants for a certain material. For example, studies show that the constants *A, B,* and *C* for water and soybean are [72, 73] : $A_{water} = 1.311$, $A_{soybean} = 1.451$, $B_{water} = B_{soybean} = 1.154\times10^4$, $C_{water} = C_{soybean} = -1.132\times10^9$ when the wavelength is in nanometers.

From the equations modeling the scattering efficiency Q_{sca} (mm^{-1}) and the scattering anisotropy factor *g*, we could see that for a particle, the scattering efficiency and scattering anisotropy is determined by its size and relative refractive index coefficient between the particle and background.

Almost all scattering media consist of many particles with different sizes. If the particles are sparsely separate from each other, the scattering from other particles within the proximity of any particle is small. Additionally, if particle separation is random, there is no systematic relationship among the phase of waves scattered by the particles. With this single scattering assumption, the total scattering within the medium is simply the sum of scattering of all individual particles. For a scattering medium, the total cross section for scattering per unit volume, or the scattering coefficient, $\mu_s(\lambda)$ and the anisotropy coefficient $g(\lambda)$ for a suspension of particles with different radii can be calculated by [73]:

$$\mu_s(\lambda) = N_0 \sum_{i=1}^{n} \sigma_{sca}(r_i, \lambda) f(r_i) \tag{2.13}$$

$$g(\lambda) = \frac{\sum_{i=1}^{n} g(r_i, \lambda)\sigma_{sca}(r_i, \lambda) f(r_i)}{\sum_{i=1}^{n} \sigma_{sca}(r_i, \lambda) f(r_i)} \tag{2.14}$$

where, σ_{sca} is the scattering cross section and is calculated by

$$\sigma_{sca} = \pi r^2 Q_{sca} \tag{2.15}$$

$f(r_i)$ is the fraction of particles with radius r_i and $\sum_{i=1}^{n} f(r_i) = 1$. N_0 is particle density and given by

$$N_0 = \frac{v}{\sum_{i=1}^{n} \frac{4}{3}\pi r^3 f(r_i)} \tag{2.16}$$

where v is the volume of scatter per unit volume of suspension.

The reduced scattering coefficient could be calculated by

$$\mu'_s(\lambda) = \mu_s(\lambda)(1 - g(\lambda)) \tag{2.17}$$

2.3.2 Empirical power law fit to reduced scattering spectrum

Instead of directly applying Mie scattering theory, van Staveren et al [73] proposed a more empirical model for reduced scattering spectrum. According to van Staveren, the scattering spectrum, such as that measured in Intralipid, was considered to satisfy a power law relationship as

$$\mu_s'(\lambda) = A\lambda^{-b} \tag{2.18}$$

where A and b are scattering amplitude and scattering power, respectively. This model has been adopted by a number of studies to characterize the spectrum of reduced scattering coefficient in the tissues [74-76]. Eqn (2.18) describes a smooth function with no oscillations in the spectrum. And the fitting process is restricted to only two parameters: the scattering amplitude *A* and the scattering power *b*. The scattering amplitude represents the scattering intensity while the scattering power describes the scattering spectrum shape.

Fig.2.7 shows the scattering spectrum of 20% Intralipid from 400-1100nm (red dots) calculated by Mie theory and the power law fit (green line) to the scattering spectrum. We could see that a power law equation as Eqn (2.18) satisfactorily describes the relationship between reduced scattering coefficient and wavelength.

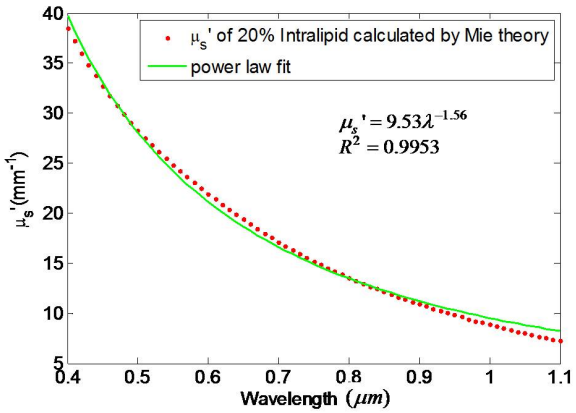

Fig. 2.7 Example of reduced scattering coefficient calculated by Mie theory and its empirical power law fit

2.3.3 Factors that influence scattering properties according to Mie theory

From the Mie theory equations, we could conclude that the scattering characteristic of the tissue is determined by the morphological characteristics of tissue, such as the scattering particles size *r* and their size distribution *f(r)* within the medium, the particle density N_0, and the relative refractive index between the scatter and background n_{rel}. In this section, the influences of these factors on scattering properties are examined.

2.3.3.1 Influence of particle size distribution

Scattering media are composed of scattering particles with different sizes distributions. For example, studies show that the histogram shape of particles size within Intralipid follows exponential decrease function. In biological tissues, the histogram shape of nuclei has been assumed to be Gaussian. However, for smaller particles, log-normal distribution has been

assumed. However, there is also a strong rationale for using a simple exponential function for the distribution of smaller particles in tissue [47].

In order to investigate the influence of size distribution function on scattering properties of a medium, the reduced scattering coefficients of media with four different kinds of particle size distribution have been simulated and compared. The average particle size within the four media is fixed to be $d = 400nm$. The total number density is set to be $N = 1 \times 10^{19} m^{-3}$. And the refractive index, which is assumed to be wavelength independent, of the background and scatter is 1.33 and 1.45, respectively. The histogram shapes of the particle size being investigated are exponentially decreasing function, step function and Gaussian distribution with narrow standard derivation (5nm) and wide standard derivation (50nm), as shown in Fig. 2.8. We could see that in the Gaussian distribution with a small standard derivation, most particles clustered around its average particle size. For Gaussian distribution with a large standard derivation, some particles spread further away from its average particle size but the majority are around its average particle size. In step distribution the particles are distributed evenly from 0 to 800nm and the exponentially decrease distribution has more particles in the smaller size range.

The reduced scattering coefficient spectra from 500 to 1000nm of media with above four size distributions calculated by Mie theory are shown in Fig. 2.9. The shape of scattering coefficient spectra changes as the size distribution changes. For example, for narrow Gaussian distribution, oscillation is observed.

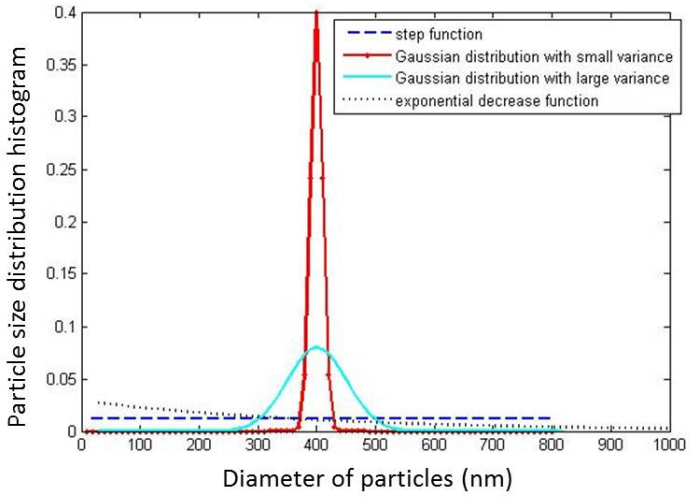

Fig. 2.8 Particle size distribution histograms

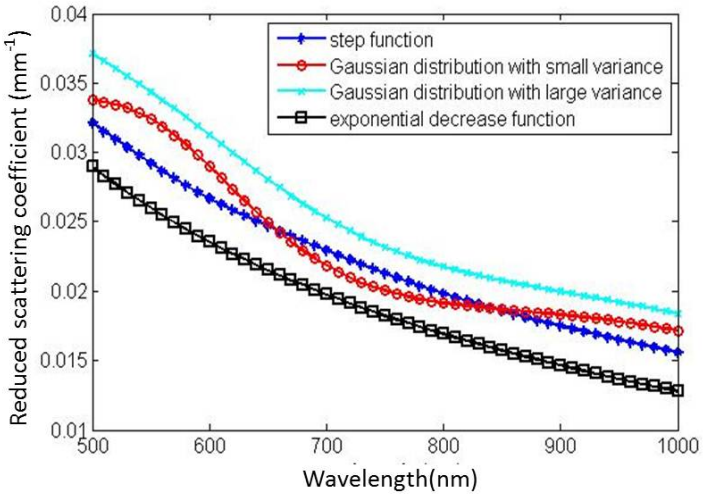

Fig. 2.9 Reduced scattering coefficient for different particle size distributions

2.3.3.2 Influence of average particle size

The influence of average particle size on the scattering properties of a medium is simulated by changing the average particle size from 50nm to 400nm while keeping the other parameters to be the same. The particle distribution is set to be exponentially decreasing function and shown in

Fig. 2.10. The particle number density is assumed to be $N = 1 \times 10^{19}\, m^{-3}$ and the refractive indices of the background and scatter are assumed 1.33 and 1.45, respectively.

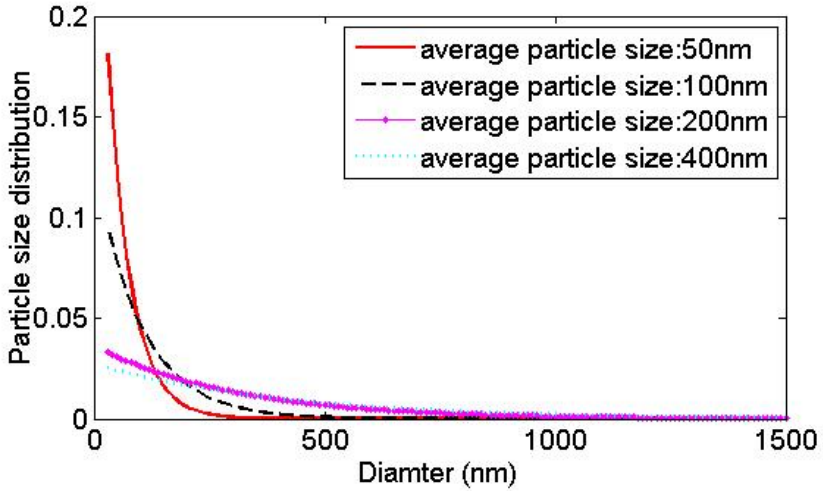

Fig. 2.10 Exponential histogram shape for different average particle sizes

In Fig. 2.11, the scattering spectra from 500 to 1000nm of media with average particle sizes to be 50nm, 100nm, 200nm and 400nm are shown. And we could see that the spectrum intensity increase as the average particle size increase.

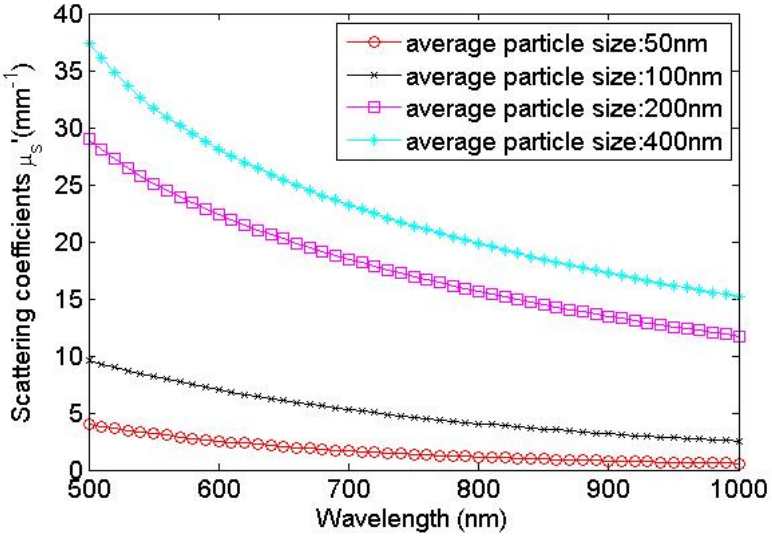

Fig. 2.11 Reduced scattering coefficient for different average particle sizes

Quantitative influence of particle size on reduced scattering coefficient spectrum could be analyzed when using power law equation to fit the scattering spectra. The fitted scattering amplitude *A* and scattering power *b* versus the average particle size is shown in Fig. 2.12 and Fig. 2.13, respectively. And we could see that the scattering amplitude increases as the particle size increases but the scattering power decreases at the same time.

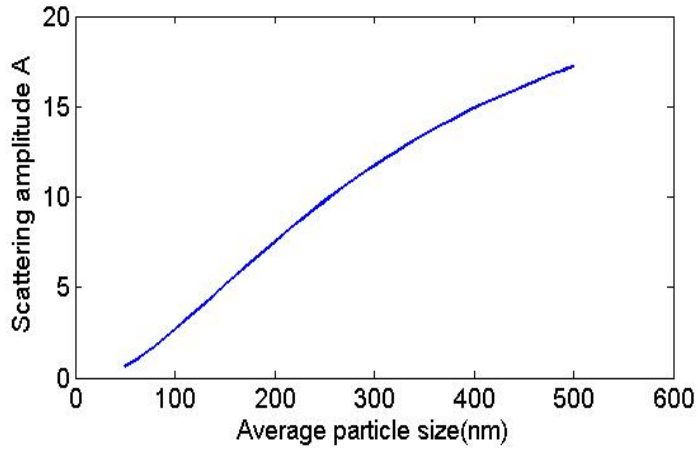

Fig. 2.12 Scattering amplitude changes as a function of average particle size

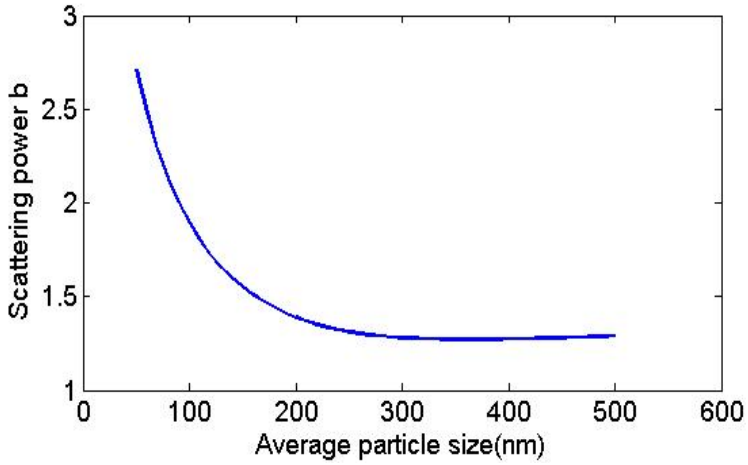

Fig. 2.13. Scattering power changes as a function of average particle size

2.3.3.3 Influence of refractive index

Refractive index is another factor that has significant effect on scattering properties of a medium. Refractive index changes slightly as wavelength changes, however, we assume it is wavelength independent for easy calculation. There is a range of indices of refraction in tissues. The extracellular fluid, which is considered as the background in most tissues, has a refractive index between 1.358 to 1.351 [77]. The refractive indices of the cytoplasm and nucleus of Chinese hamster cells have been measured to be 1.3703 and 1.392, respectively [78]. Lipid and proteins have higher refractive indices, which are 1.46 [79] and 1.51[80], respectively.

The refractive index influences scattering spectrum in the form of relative refractive index, or the scatter's refractive index over the background's refractive index. In order to see the influence of refractive index on scattering properties, Mie simulation is done by keeping the other parameter constant but changing the relative refractive index. The background refractive index is fixed to be 1.33 and the refractive index of scatter is changed from *1.4 to 1.6*, which corresponding to relative refractive index n_r changing from *1.05* to *1.2*. Fig.2.14 shows the scattering spectrum for relative refractive indices to be 1.05, 1.1, 1.15 and 1.2 when the average particle size to be *400nm* with exponential distribution and the particle density to be $1\times10^{19}\,m^{-3}$. And we could see that the intensity of reduced scattering coefficients increases as the relative index increase.

When using power law equation to fit the scattering spectrum, we could get the scattering amplitude *A* and scattering power *b* for different relative refractive index, as shown in Fig. 2.15 and Fig. 2.16, respectively. Unlike the particle size, which makes the scattering amplitude and scattering power change in opposite directions, the refractive index increase results in increasing in both scattering power and scattering amplitude.

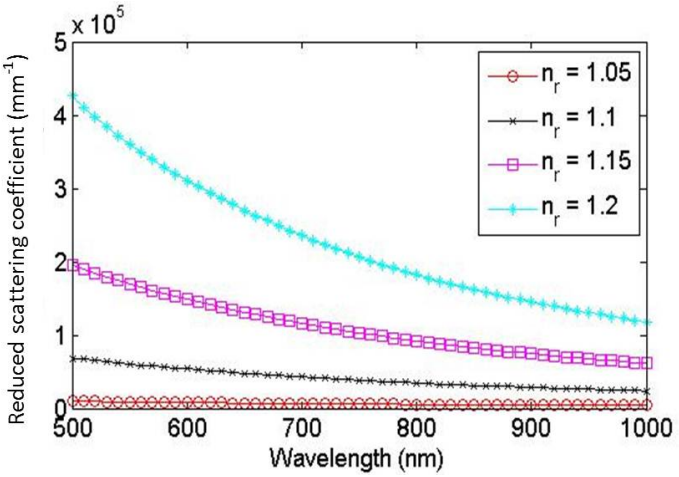

Fig. 2.14 Reduced scattering coefficient for different relative refractive indices

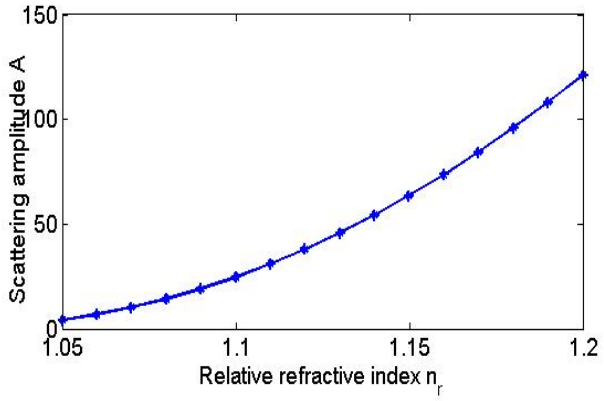

Fig. 2.15 Scattering amplitude changes as a function of relative refractive index

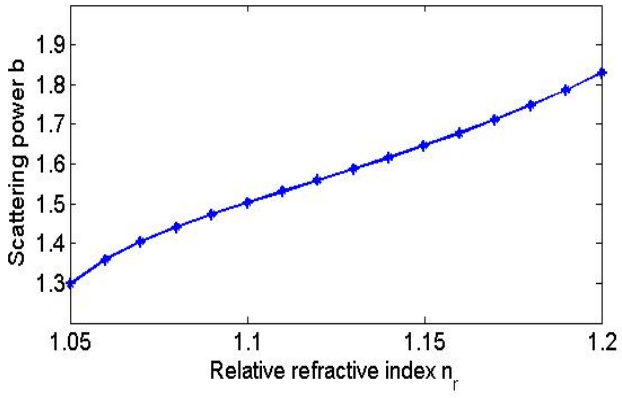

Fig. 2.16 Scattering power changes as a function of relative refractive index

2.3.3.4 Influence of particle density

The influence of particle density on the scattering spectrum could be well estimated by Mie theory equations. The intensity of scattering spectrum is linear to the particle density but the shape of scattering spectrum has no relationship with the particle density. And this estimation is confirmed by Fig. 2.17 and Fig. 2.18, which show the scattering amplitude and scattering power changes as the particle density changes, respectively. In the simulation, the average particle size is *200nm*, the relative refractive index is 1.1 and the particle distribution follow exponential decrease function.

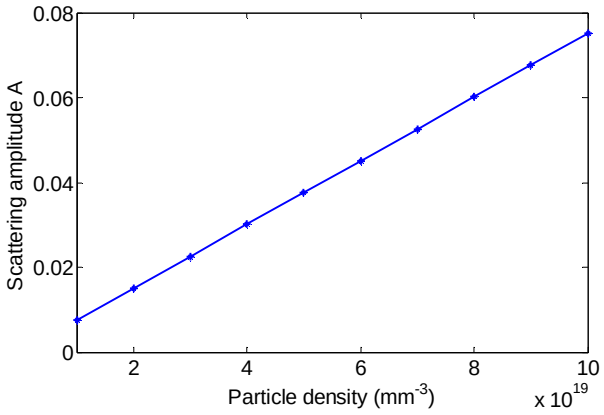

Fig. 2.17 Scattering amplitude changes as a function of particle density

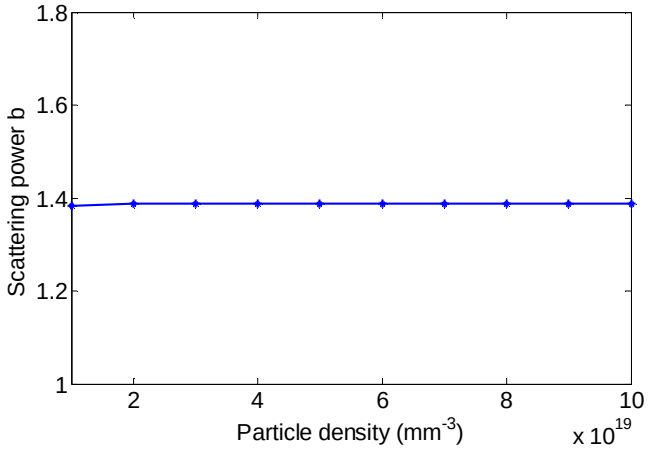

Fig. 2.18 Scattering power changes as a function of particle density

However, Mie theory is based on the assumption of independent scattering. In reality, the light interaction with particles is composed of multiple internal reflections and redirections from multiple particles and the scattering is dependent of the relative position of particles [81]. Therefore the linear relationship between the scattering amplitude and particle density is observed only when the particle density is small. As the particle density increase, the dependent scattering effects could not be neglected and the increase of scattering amplitude could not catch up with the increase of particle density.

.

CHAPTER III

INSTRUMENTATION

Reflectance spectroscopy has the potential to distinguish the normal and degenerated intervertebral disc. Considering the anatomical structure of the nucleus pulposus in a canine intervertebral disc, single fiber reflectance spectroscopy system is proposed for canine intervertebral disc evaluation. In this chapter, the configuration of single fiber reflectance spectroscopy system will be introduced. We will discuss several advantages of using single fiber reflectance spectroscopy for this study. The system will also be evaluated from several aspects, including the source spectrum, the spectrometer wavelength calibration, the spectrum calibration and the system stability.

3.1 Configuration of single fiber based reflectance spectroscopy system

The configuration of the needle-based signal-fiber reflectance spectroscopy system is illustrated in Fig. 3.1. As shown in Fig. 3.1(a), by using a bifurbrated fiber, the light source and detector were integrated into a signal fiber and inserted into sample via a spinal needle. The VIS/NIR light was generated by a compact deuterium tungsten light source (L10671, Hamamatsu Photonics, Japan) coupled with a 940nm light-emitting-diode (LED) (M940L2, Thorlabs, NJ, USA). Each of the two light sources was coupled to one branch of 200μm core-diameter bifurcated fiber *A* (BIF200-VIS/NIR, Ocean Optics Inc, USA) to integrate the spectra of the two light sources at the

combining branch. The combining branch of fiber bundle *A* was coupled to one branch of 400µm core-diameter bifurcated fiber *B* (BIF400-VIS/NIR, Ocean Optics Inc, USA), the other branch of which was connected to a spectrometer (VIS-NIR Hyperspectral USB Spectrometer, NT58-303, Edmund Optics Inc, NJ, USA). The combining branch of the fiber bundle *B* was connected to a standard PLDA fiber of 320µm core-diameter (fiber *C* shown in Fig.3.1 (b), H320R, New Star Lasers, Inc, CA, USA). The fiber *C*, which is identical to that being used in PLDA, was placed in the tissue by inserting through a twenty gauge myelegraphic spinal needle. In order to minimize the back reflection at the tip of fiber, fiber C was polished to an angle of 15 degrees, as shown in Fig. 3.1 (a) [14].

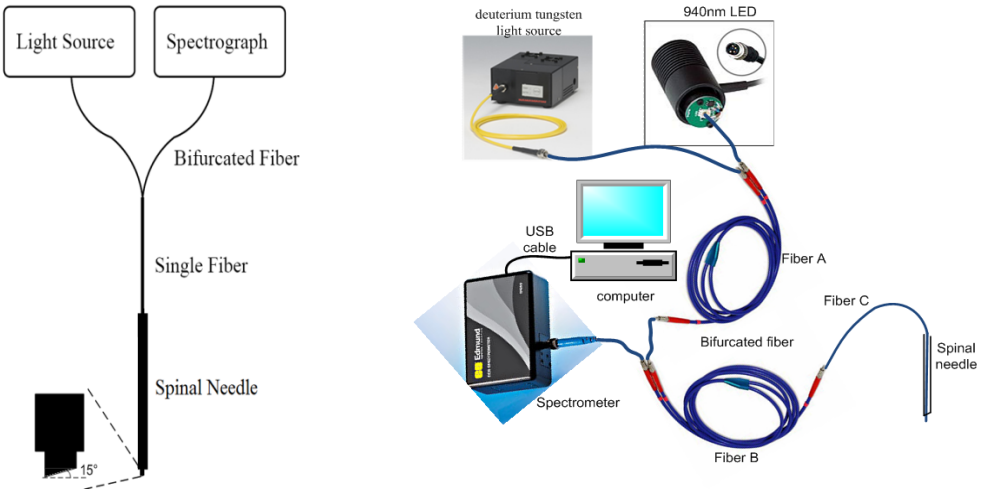

(a)Schematic configuration (b) Experimental configuration

Fig. 3.1 Configuration of needle-based single fiber reflectance spectroscopy

3.2 Advantages of single fiber reflectance spectroscopy

There are several advantages of using single fiber reflectance spectroscopy system for the evaluation of canine intervertebral disc degeneration.

First, single fiber reflectance spectroscopy system is suitable for the anatomy structure of nucleus pulposus within canine intervertebral disc. The nucleus pulposus is confined by outer layer

annulus fibrosus and surrounding vertebrae. Therefore it forms a “shallow-and-small-slab” geometry with a thickness of approximately a few millimeters and diameter of no more than several centimeters, as shown in Fig. 3.2. Single fiber reflectance system could be incorporated with the spinal needle and delivered to the small volume of nucleus pulposus. Additionally, the single fiber reflectance system is sensitive to local optical properties, so the influence from the surrounding tissues on the detected optical spectrum could be minimized.

Second, single fiber configuration could be easily integrated into needle fiber based PLDA clinical application. Using the same sampling fiber and spinal needle as PLDA, the single fiber reflectance spectroscopy system can be operated in conjunction with PLDA.

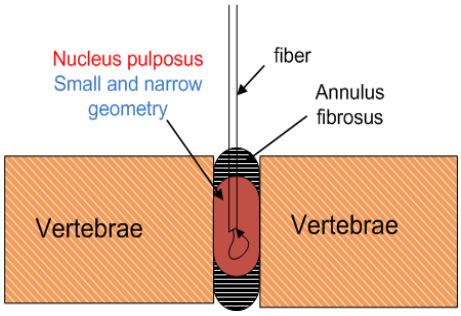

Fig. 3.2 Illumstation of the “shallow-and-small-slab” geometry of nucleus pulposus

3.3 System evaluation

3.3.1 Source spectrum

The deuterium tungsten light source L10671 is composed of one small deuterium lamp and one 0.5W tungsten lamp, which has a combined spectrum distribution from 200nm to 1600nm. The typical spectrum of L10671 specified by manufacturer is shown in Fig. 3.3(a) [82]. However, due to the non uniform spectrum response of the VIS-NIR spectrometer, the measured spectrum (smoothed by a Savitzky-Golay smoothing filter (SG filter)) is shown as Fig. 3.3 (b). Since the spectrometer has low response to ultraviolet light, we shut down the deuterium lamp. And we could see that the spectrum intensity decreases as the wavelength increases after 600nm. In order

to recover more water information, a 940nm LED is integrated into the light source to inhance the spectrum intensity at around 940nm.

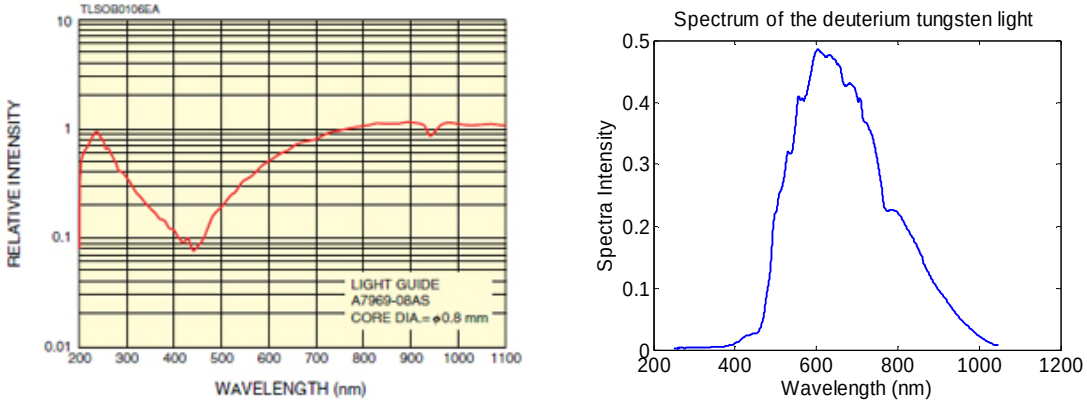

(a) Spectrum specified by manufacturer (b) Measured spectrum

Fig. 3.3 Deuterium tungsten light source spectrum

3.3.2 Wavelength calibration

The spectrometer used in our system is a VIS-NIR hyperspectral USB Spectrometer, with spectrum range of 350-1100nm and step size varies from 0.27nm to 0.53nm. In order to calibrate the wavelength of the spectrometer, we compared the measured peaks of commercial fluorescence light source with the known peaks of the mercury, terbium, and europium filled in it. The spectrum of fluorescence light source measured by the NT58-303 spectrometer is shown in Fig. 3.4. Twenty peaks were recognized by the spectrometer between 400 and 720nm. The measured peak positions and the known peak positions [83] are shown in Table 3.1. Among the twenty peaks recognized by spectrometer, peak 3 is broad and it's hard to tell its exact wavelength form the measured spectrum, so peak 3 is discarded.

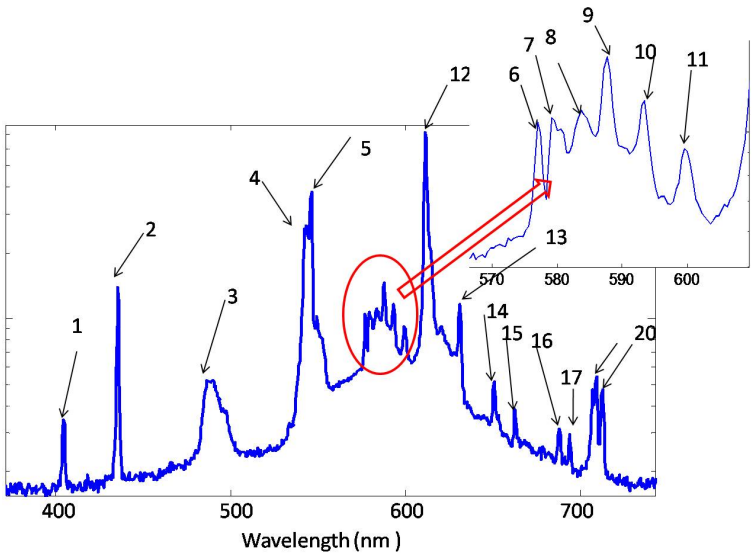

Fig. 3.4 Measured spectrum of fluorescence light source

Table 3.1 Compare the theoretic and measured peak positions of fluorescence light source

Peak Number	Wavelength of Peak (nm) [83]	Measured Peak wavelength (nm)	Peak Number	Wavelength of Peak (nm) [83]	Measured Peak wavelength (nm)
1	405.4	404.48	11	599.7	599.57
2	436.6	435.77	12	611.6	611.41
3	487.7	486.5 to 489.8	13	631.1	631.38
4	542.4	543.53	14	650.8	650.65
5	546.5	546.27	15	662.6	662.50
6	577.7	576.95	16	687.7	687.98
7	580.2	579.18	17	693.7	693.76
8	584.0	583.64	18	707	707.28
9	587.6	587.63	19	709	709.32
10	593.4	593.39	20	712.3	712.57

Fig. 3.5 shows the wavelength difference between the measured peaks and the theoretic peaks at the theoretic peak positons (blue *). The two red lines within Fig. 3.5 show the wavelength resolution of the spectrometer at given wavelength. From Fig. 3.5 we could see that most of

wavelength errors are within the spectrometer resoulution. Therefore the wavelength accuracy of the spectrometer used in our system is satisfactory between 400 and 720 nm range. And it is reasonable to assume that the wavelength accuracy at higher wavelength range has the same acuuracy.

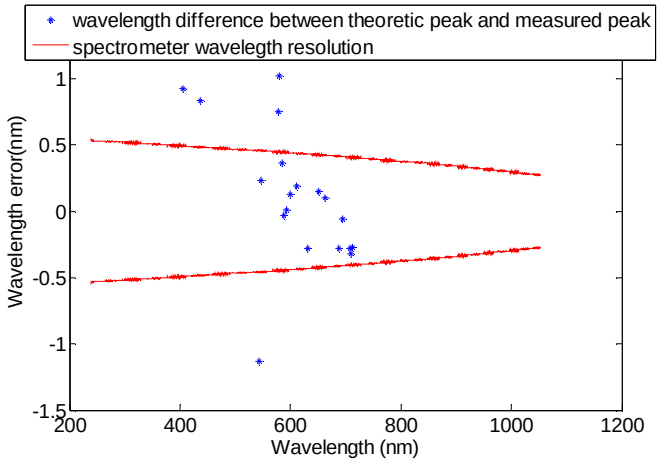

Fig. 3.5 Peak positon errors compared with the resolution of spectrometer

3.3.3 Spectrum calibration

For single fiber configuration, the reflectance spectrum comes from the single or elastic scattering. Studies show that for single fiber reflectance spectroscopy, the reflectance spectrum is modeled by [4-6, 18]

$$R = a\mu_s' e^{-\mu_a L} \tag{3.1}$$

The single fiber reflectance spectrum is linear to the reduced scattering coefficient of the medium and the attenuation due to absorption within the medium is modeled by Lambert-Beer law.

However, due to reflections from the fiber tip as well as from multiple stages of fiber connections within the system, additional terms other than reflectance from the sample could be collected by the spectrometer. Some techniques, such as polishing the fiber tip to 15 degree, could minimize, but not fully eliminate, the back reflection at the tip of the sample fiber. Therefore, a base line

spectrum was measured by the spectrometer even in non-scattering medium, such as in air and water. Mixed with the spectrometer responses characteristic and source output spectrum, the base line spectrum measured in air is shown in Fig. 3.6. When we compared the tungsten light spectrum in Fig. 3.3(b) and base line spectrum in Fig. 3.6, the reflectance spectrum in the air showed a slightly different shape from the source spectrum. The difference is presumablely caused by the wavelength response characteristics of the fibers used in the reflectance spectroscopy system, which confirms the existence of internal reflectance.

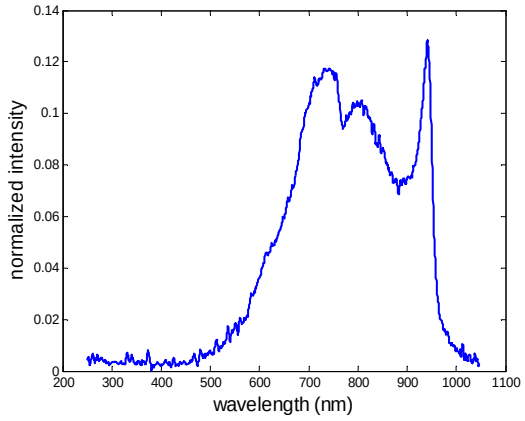

Fig. 3.6 Base line spectrum in non scattering medium (In air).

When the fiber tip is placed in scattering medium, the measured spectrum contains not only the reflectance spectrum from the samples, but the base-line information. In order to decouple the internal-reflection and back reflection as well as the source profile and spectrometer responsive charicteriscs from the measured spectrum, Eqn (3.2) is used to calibrate the spectrum.

$$R(\lambda) = \frac{R_{sample}(\lambda) - R_{water}(\lambda)}{R_{air}(\lambda) - R_{water}(\lambda)} \tag{3.2}$$

Here, $R(\lambda)$ is the calibrated spectrum. $R_{sample}(\lambda)$ refers to the measurement from the scattering sample, as shown in Fig. 3.7 (a). And $R_{water}(\lambda)$ and $R_{air}(\lambda)$ refer to the measured spectra when placing the sensor fiber in no scattering media, water and air, respectively, as shown in Fig. 3.7

(b). The calibration procedure involves the measurements from scattering sample as well as from non scattering water and air. And all the measurements were done in the dark environment to eliminate influence from the ambient light.

Fig. 3.7 Illustration of reflecance from scattering medium and non scttering medium

In scattering medium, the measured spectrum could be modeled by,

$$R_{sample}(\lambda) = \eta(\lambda)\left[(a\mu'_s(\lambda))e^{-\mu_a(\lambda)L}\varphi(\lambda) + \eta_{samplefiber}\varphi(\lambda) + \gamma(\lambda)\times\varphi_s(\lambda)\right] \tag{3.3}$$

where $\varphi(\lambda)$ is the input spectrum profile at the fiber tip, $\eta_{samplefiber}$ is the refractive index mismatch between the fiber and the sample, $\gamma(\lambda)$ represents the inter-fiber reflectance efficiency, which is wavelength dependent, $\varphi_s(\lambda)$ is the source profile; and $\eta(\lambda)$ represents the response characteristic of the spectrometer. Therefore, the reflectance spectrum is composed of three parts: the reflectance from the sample, the back reflection at the fiber tip, and the internal reflectance within the fiber connector.

In non-scattering medium such as in water or in air, the reflectance spectra is modeled differently from scattering medium, due to the dominant specular reflection, as

$$R_{water}(\lambda) = \eta(\lambda)[\eta_{waterfiber}\varphi(\lambda) + \gamma(\lambda)\times\varphi_s(\lambda)] \tag{3.4}$$

$$R_{air}(\lambda) = \eta(\lambda)[\eta_{airfiber}(\lambda)\varphi(\lambda) + \gamma(\lambda)\times\varphi_s(\lambda)] \tag{3.5}$$

where $\eta_{waterfiber}$ and $\eta_{airfiber}$ are the water/fiber and air/fiber index mismatch, respectively.

Substituting Eqns. (3.3)-(3.5) into Eqn. (3.2), we have

$$\begin{aligned} R(\lambda) &= \frac{R_{sample}(\lambda) - R_{water}(\lambda)}{R_{air}(\lambda) - R_{water}(\lambda)} \\ &= \frac{\eta(\lambda)[(a\mu'_s(\lambda))e^{-\mu_a(\lambda)L}\varphi(\lambda) + \eta_{samplefiber}\varphi(\lambda) + \gamma(\lambda)\times\varphi_s(\lambda)] - \eta(\lambda)[\eta_{waterfiber}\varphi(\lambda) + \gamma(\lambda)\times\varphi_s(\lambda)]}{\eta(\lambda)[\eta_{airfiber}\varphi(\lambda) + \gamma(\lambda)\times\varphi_s(\lambda)] - \eta(\lambda)[\eta_{waterfiber}\varphi(\lambda) + \gamma(\lambda)\times\varphi_s(\lambda)]} \\ &= \frac{(a\mu'_s(\lambda))e^{-\mu_a(\lambda)L} + \eta_{samplefiber} - \eta_{waterfiber}}{\eta_{airfiber} - \eta_{waterfiber}} \\ &= \alpha\mu_s'(\lambda)e^{-\mu_a(\lambda)L} + \beta \end{aligned} \tag{3.6}$$

We observed that by calibration, the effects of source profile, nonuniform response of spectrometer and fiber-transmission characteristics have been suppressed, and the back reflectance becomes a constant.

Fig. 3.8 shows the original measured spectrum (Fig. 3.8(a)) and its calibrated spectrum (Fig. 3.8(b)) of 10% Intralipid. The calibrated spectrum is too noisy outside the range between 500nm and 950nm and has been discarded. And we could see a relative flat spectrum after calibration, which is representative of the optical properties of the medium.

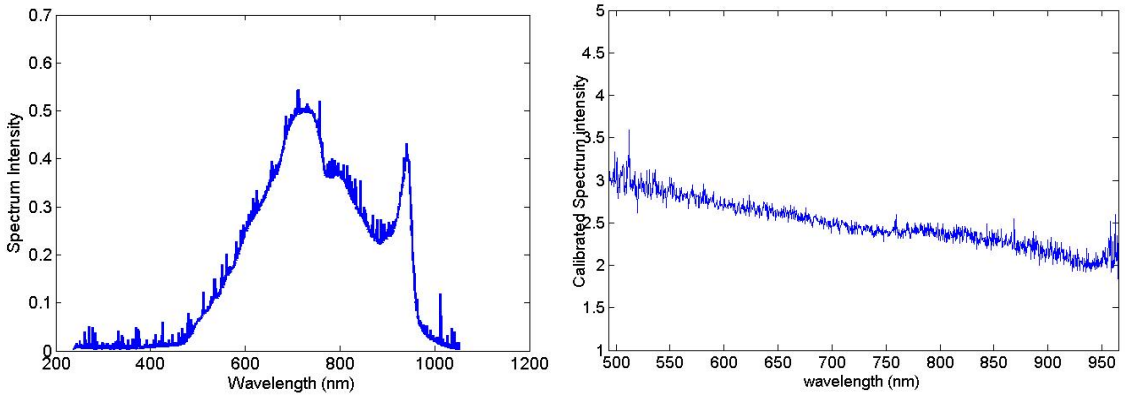

(a)Original spectrum (b) Calibrated spectrum

Fig. 3.8 Original spectrum and calibrated spectrum of 10% Intralipid

3.3.4 Spectrum stability

Without source and detector stabilization technique applied to our system, there were expected to be some instabilities in the measured spectrum. Fig. 3.9 (a) shows the standard deviation of water, air and 10% Intralipid spectrum within 500nm to 950nm in two hours' time span.

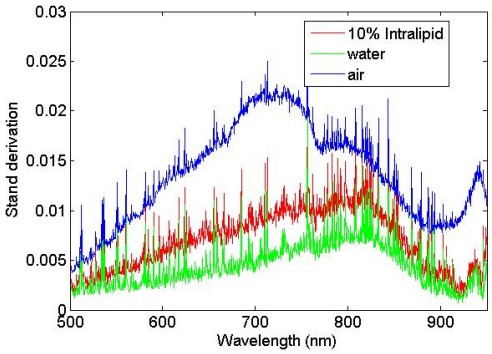

Fig. 3.9 Standard derivation of 10% Intralipid, water and air spectra within two hour time span

According to the propagation of uncertainty,

Given

$$X = f(A, B, C, ...)$$
$$\sigma_x = \sqrt{(\frac{\partial f}{\partial A}\sigma_A)^2 + (\frac{\partial f}{\partial B}\sigma_B)^2 + (\frac{\partial f}{\partial C}\sigma_C)^2 + \mathrm{L}} \tag{3.7}$$

the standard derivation of the calibrated spectrum could be expressed as

$$\begin{aligned}\sigma_R &= \sqrt{(\frac{\partial R}{\partial R_{sample}}\sigma_{R_{sample}})^2 + (\frac{\partial R}{\partial R_{water}}\sigma_{R_{water}})^2 + (\frac{\partial R}{\partial R_{air}}\sigma_{R_{air}})^2} \\ &= \sqrt{(\frac{1}{R_{air} - R_{water}}\sigma_{R_{sample}})^2 + (\frac{R_{air} + R_{sample} - 2R_{water}}{(R_{air} - R_{water})^2}\sigma_{R_{water}})^2 + (\frac{R_{sample} - R_{water}}{(R_{air} - R_{water})^2}\sigma_{R_{air}})^2}\end{aligned} \tag{3.8}$$

When implementing Eqn (3.8), the standard derivative of calibrated 10% Intralipid are shown as Fig. 3.10. In Fig. 3.11 the standard derivation and its average spectrum of 10% Intralipid is shown.

From Fig. 3.11 we could see that when ignoring the high frequency noises, which could be eliminated by smoothing, the calibrated spectrum has an approximate 30% fluctuation from its average value. Due to the instability of the spectrum signal, accurate quantitative calculation is challenging.

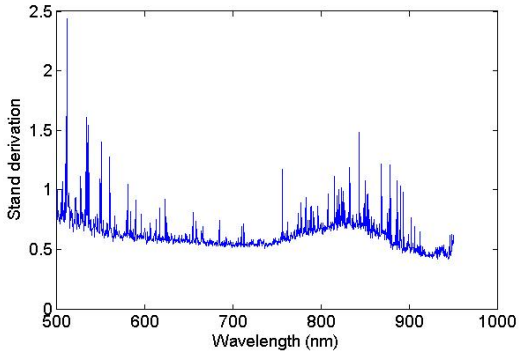

Fig. 3.10 Standard derivation of calibrated 10% Intralipid spectrum

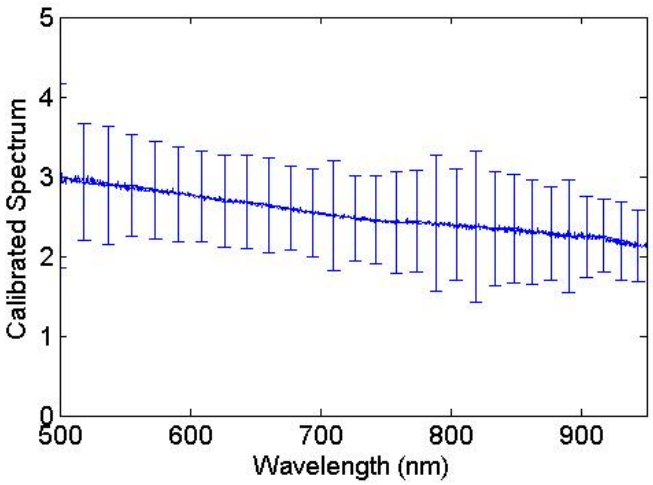

Fig. 3.11 Average calibrated 10% Intralipid spectrum with standard derivation

3.3.5 Photon path length and sampling depth

The modeling of sampling depth and photon path length is very important for measurements and quantitative calculation. For this study, the intervertebral disc is typically no more than several centimeters in diameter (depending on the size of dog) and a couple of millimeters in thickness,

the nucleus pulposus within the intervertebral disc forms a “shallow-and-small-slab” geometry that is challenging for the reflectance measurement. It is therefore imperative to estimate if the surrounding annulus fibrosus and vertebrae have significant effects on the reflectance spectrum.

Kanick, et al [14, 17] modeled the sampling depth *Z* and path length *L* for single fiber reflectance spectroscopy system based on phantom experiments and Monte Carlo simulation. According to their studies, the sample depth *Z* and photon path length *L* are determined by the optical properties of the medium and the diameter of the fiber used in single fiber reflectance system. And they gave analytical models for *L* and *Z* that have been validated for 550 - 800nm wavelength range, and for absorption coefficient $\mu_a = [0.1-3]mm^{-1}$, reduced scattering coefficient $\mu_s' = [0.2-4]mm^{-1}$, and fiber diameter $d = [0.2-2]mm$.

$$L = \frac{1.34de^{0.17d}}{(\mu_s' d)^{0.23}(0.52 + (\mu_a d)^{0.52})} \tag{3.9}$$

$$Z = \frac{0.38e^{-0.06\mu_a d}}{(\mu_s' d)^{0.12}} L \tag{3.10}$$

In this study, the diameter of the fiber is fixed to be $d = 0.32mm$. Our interested wavelength range (500 – 950nm) is wider than Kanick’s study. Moreover, the absorption coefficient is expected to be no more than $1mm^{-1}$ since the absorption coefficient of water, the main absorber within the intervertebral disc nucleus pulposus, is low within 500-950nm wavelength range. Although there are differences in wavelength range and expected optical properties, Kanick’s models for *L* and *Z* are still believed to work for our situation. We use the empirical models given in Eqns. (3.9) and (3.10) to calculate the path length and sampling depth $u_a = [0.0001-1]mm^{-1}$, $u_s' = [0.2-2]mm^{-1}$, and $d = 0.32mm$, as shown in Fig. 3.12. The indications in Fig. 3.12 agree with the physical fact that light penetrates deeper and experiences longer path-length as the scattering and absorption coefficients decrease. It is estimated from Fig. 3.12 that when the reduced scattering and absorption coefficients are $0.4mm^{-1}$ and $0.001mm^{-1}$, the sampling depth

and photon path-length for a 0.32mm fiber is approximately 0.68 *mm* and 1.4 *mm*, respectively. This implies that if the fiber is placed in the middle of the nucleus, the interference of the surrounding annulus fibrosus and vertebrae on the measurement is insignificant.

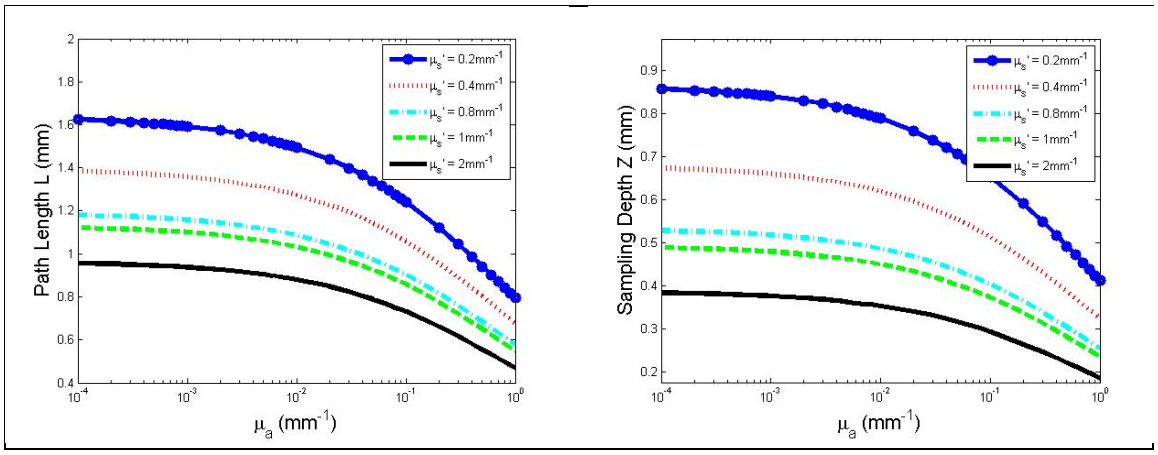

(a) Path length of the photon (b) Sample depth

Fig. 3.12 Path length and sampling depth of signal fiber spectroscopy

CHAPTER IV

PHANTOM STUDIES

We have modeled the calibrated reflectance spectrum as linear to the reduced scattering coefficient of the medium while being attenuated by its absorption. And in this chapter, Intralipid phantom studies have been performed to validate this model.

Intalipid is a kind of phantom that is proposed to have similar optical properties as the nucleus pulposus, which has high scattering and low absorption. The scattering properties of Intralipid are well known and the absorption comes from lipid and water. In this chapter, the component and properties of Intralipid are introduced. The preparation of the Intralipid phantom and the experimental procedure are discussed. The results from Intralipid phantoms are shown and analyzed.

Polystyrene phantoms with different average particle sizes are also been tested. The simulated reduced scattering coefficient spectra by Mie theory and the measured reflectance spectra from polystyrene phantoms were compared.

4.1 Intralipid phantoms

4.1.1 Introduction to Intralipid

Intralipid is a brand name for an aqueous suspension of lipid droplets that is sterile and suitable for patients who are unable to get nutrition via an oral diet. It is an emulsion of soy bean oil, egg

phospholipids and glycerin and available in 10%, 20% and 30% concentrations [84]. Intralipid is also widely used in optical experiments to simulate the scattering properties of biological tissues. Appropriate concentration of Intralipid has similar scattering coefficient as biological tissues and can simulate the tissue light interaction at red and near-infrared light wavelength ranges where tissue is highly scattering but has a rather low absorption coefficient.

Intralipid is composed mostly of water and soybean oil. According to the manufacturer, 500mL Intralipid-20% contained 100g fractionated soybean oil, 6g lecithin and 11.25g glycerol, that is 107.88mL, 5.82mL, and 8.92mL, respectively.

The glycerol is dissolved into water molecules and does not scatter light. There is no measurable influence on the scattering parameters between the glycerol water solution and pure water [73]. The scatter within Intralipid is the soybean oil encapsulated by an approximately *2.5-5nm* monolayer membrane of lecithin [85]. Assuming that lecithin has the same refractive index as soybean oil and it does not absorb light at the investigated wavelength; the influence of lecithin shell on scattering could be negligible. However, the volume occupied by lecithin was included when calculate the particle size. The particle size of Intralipid is measurable using transmission electron microscopy. Staveren [73] measured the particle size of 10% Intralipid to be exponentially decreasing with 97nm mean particle size, as shown in Fig. 4.1.

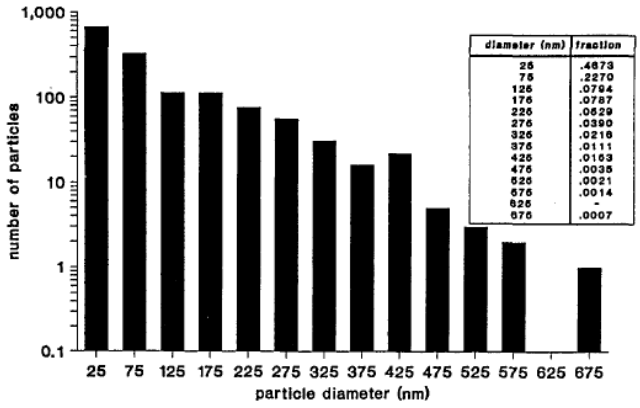

Fig. 4.1 Particle size distribution of 10% Intralipid measured by Staveren [73]

Calculated by Mie theory, the reduced scattering coefficient of Intralipid is proportional to its concentration. However, as discussed in section 2.3, the Mie theory is based on the assumption of independent scattering in which the influence of the neighboring scatter is neglected. Therefore when considering the influence from the surrounding scatters, which increases as the concentration increases, the linear relationship between the Intralipid concentration and its reduced scattering coefficient doesn't apply. Zaccanti et al [48] proposed an empirical relationship between the reduced scattering coefficient and the concentration of Intralipid at 632.8nm wavelength:

$$\mu_s' = 127.0c - 205.3c^2 \tag{4.1}$$

where the reduced scattering coefficient μ_s' is in mm^{-1}. This relationship for up to 20% Intralipid is shown in Fig.4.2. We could see that at low concentration, the reduced scattering coefficient of Intralipid is approximately linear to its concentration.

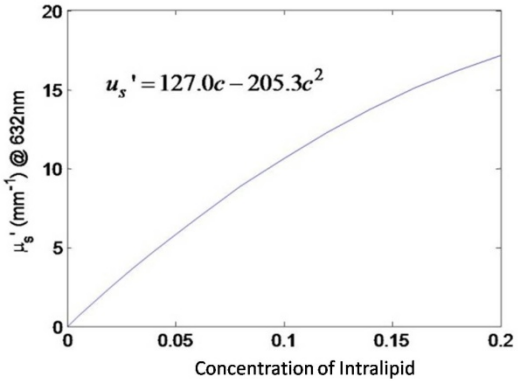

Fig. 4.2 Reduced scattering coefficient of Intralipid at 632nm v.s. its concentration.

The absorber within Intralipid is lipid and water, whose molar extinction coefficients are shown in Fig. 4.3. For different concentrations Intralipid, the absorption coefficients could be expressed as

$$u_a = c * u_{a\_lipid} + (1-c) * u_{a\_water} \tag{4.2}$$

where c is the concentration of Intralipid and u_{a_lipid} and u_{a_water} are the absorption coefficients of lipid and water, respectively. Fig. 4.4 shows the absorption coefficients of 1% (black solid line) and 20 % (red dash line) Intralipid. And we could see that the absorption coefficient changes little as the concentration changes. Within the range of 500 to 700 nm, the absorption of Intralipid is negligible, and the Intralipid could be seen as a pure scattering medium. However, the absorption from lipid and water may play a significant role when the wavelength is higher than 700nm.

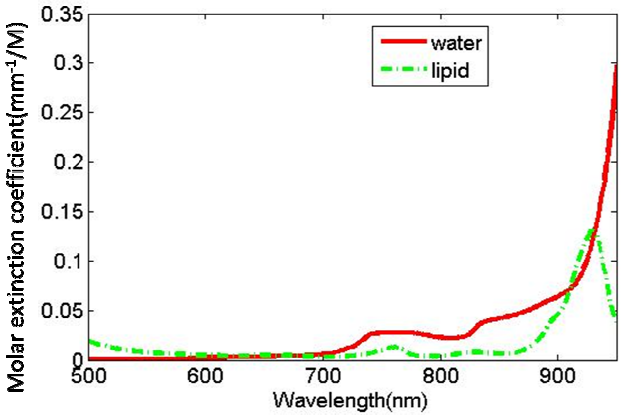

Fig. 4.3 Absorption coefficients of water and lipid. Data are obtained from [20, 21]

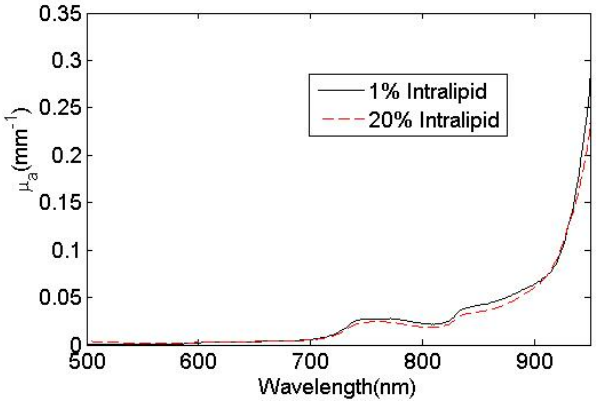

Fig. 4.4 Absorption coefficients of 1% and 20% Intralipid

4.1.2 Phantom preparation and experimental procedure

The Intralipid phantoms used in our study were diluted with reagent grade water from 20% Intralipid (Fresesnius Kabi, Uppsala, Sweden). The total volume of each Intralipid phantom was

10 ml with volume concentrations to be 0.5%, 1%, 2%, 3%, 4%, 5%, 6%, 8%, 10%, 12%, 14%, 16%, 18%, and 20%, respectively. The reflectance spectra of Intralipid were measured after dilution. Four rounds of measurements have been done to make sure the results are repeatable. Two of the measurements were done by the sequence from 0.5% to 20%, and the other two were from 20% to 0.5%. Before each round of measurements, the spectra of reagent grade water and air were collected for calibration.

4.2 Results of Intralipid phantom experiments

The reflectance spectra of Intralipid from 0.5% to 20% are shown in Fig. 4.5. The spectra have been calibrated using Eqn (3.6) to reduce the influence from source spectrum, spectrometer response characteristic, and internal and back reflectance, and smoothed using 100 point smoothing algorithm to depress noise. We could see that the intensity of the reflectance spectrum increase as the concentration increases. And also the shape of the calibrated spectrum is approximately inversely linear to the wavelength. The spectrum intensity as a function of scattering coefficient and spectrum shape change as the function of wavelength will be studied in the following sections.

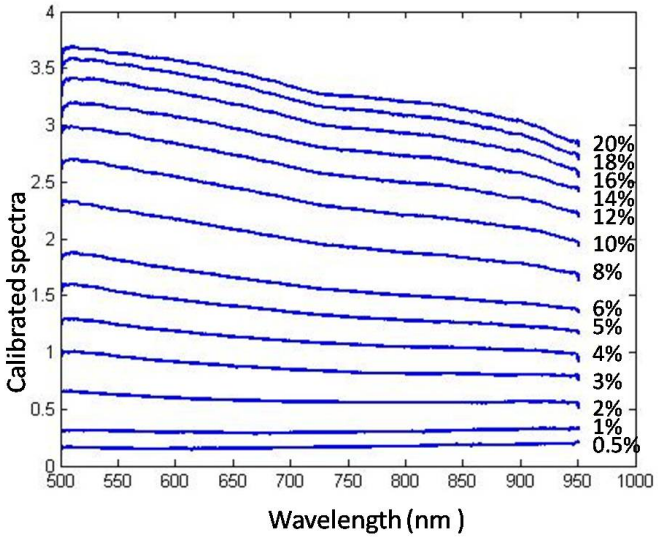

Fig. 4.5 Calibrated reflectance spectra of Intralipid at different concentrations

4.2.1 Relationship between spectrum intensity and reduced scattering coefficient

The relationship between the Intralipid spectrum intensity and its reduced scattering coefficient is shown in Fig. 4.6. The x axis is the reduced scattering coefficient of Intralipid at 632nm, which is calculated by Eqn (4.1) from its concentration. The y axis is the average spectrum intensity from 500 to 950nm. In Fig. 4.6 (a), the results from four sets of tests are shown. As expected, there are discrepancies among different sets of the test due to instability of the signal. However, when we normalized the average spectrum intensity at 20%, as shown in Fig. 4.6 (b), all four curves are coincident with each other illustrating the same trend. The spectrum intensity is approximately linear to the reduced scattering coefficient of Intralipid.

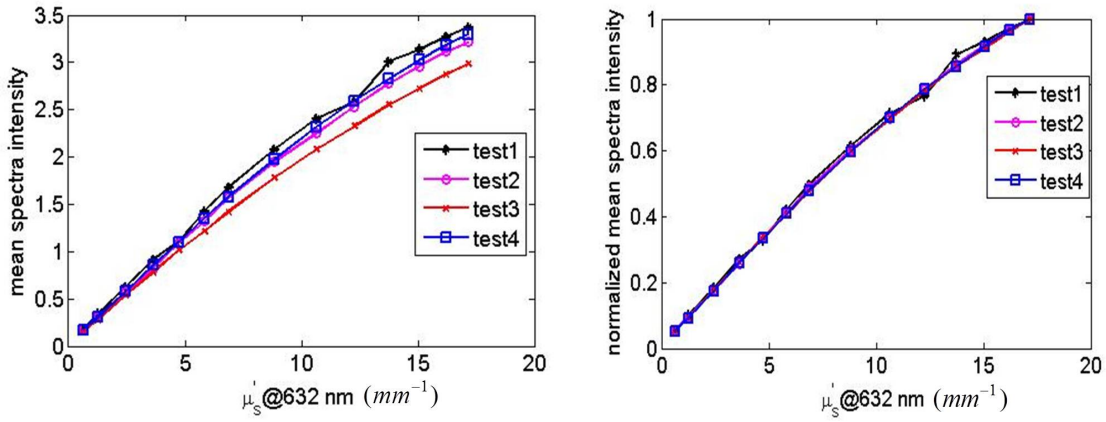

(a) Mean spectrum (b) Normalized mean spectrum

Fig. 4.6 Mean spectrum intensity vs. reduced scattering coefficient.

A linear fit to the normalized mean spectrum intensity is shown in Fig. 4.7. The red * shows the normalized Intralipid spectrum intensity averaged over the four rounds of tests. And the green line shows the linear fit to the data described as $R_{norm} = 0.058\mu_s' + 0.0524$ with the coefficient of determination $R^2 = 0.9928$. According to Eqn (3.6), the calibrated spectrum $R \propto \mu_s' e^{-\mu_a L}$. Since Intralipid is scattering dominant, the absorption could be neglected, or $\mu_a = 0$. Then we could see that the reflectance spectrum of Intralipid is linear to the reduced scattering coefficient

theoretically. And the linear relationship between spectrum intensity and reduced scattering coefficient shown in Fig. 4.7 agrees with our calibrated reflectance spectrum model. And we could also notice from Fig. 4.7 that the linear relationship between spectrum intensity and reduced scattering coefficient could be approximately seen as proportional relationship since the intersection is small.

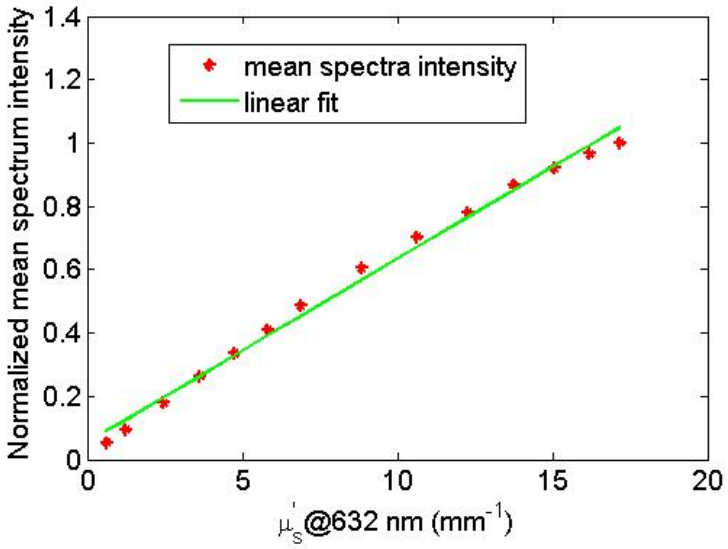

Fig. 4.7 Linear fit to the mean spectrum intensity of Intralipid

4.2.2 Wavelength dependent reflectance spectrum

As discussed in the previous section, the reflectance spectrum is proportional to its reduced scattering coefficient. Reduced scattering coefficient is wavelength dependent and described as a empirical power law equation as shown in Eqn (2.18). Therefore the reflectance spectrum should follow the same relationship, as

$$R(\lambda) = \alpha\mu_s'(\lambda)e^{-\mu_a(\lambda)L} = A\lambda^{-b}e^{-\mu_a(\lambda)L} \tag{4.3}$$

If the absorption is neglected, the reflectance spectrum follows the exponentially decrease equation, as

$$R(\lambda) = A\lambda^{-b} \tag{4.4}$$

Fig. 4.8 shows the reflectance spectrum of 20% Intralipid (red dash line) and its power law fit (green solid) to the spectrum between 500 to 700nm range, where the absorption of Intralipid could be safely neglected. And the fitted power law equation is extended to 950nm. Fig. 4.8 shows that the reflectance spectrum of Intralipid follows the power law equation perfectly within 500 to 700nm range. Beyond 700nm, the reflectance spectrum separates from the fitted power law relationship a little bit, which is caused by absorption of Intralipid and will be discussed in next section.

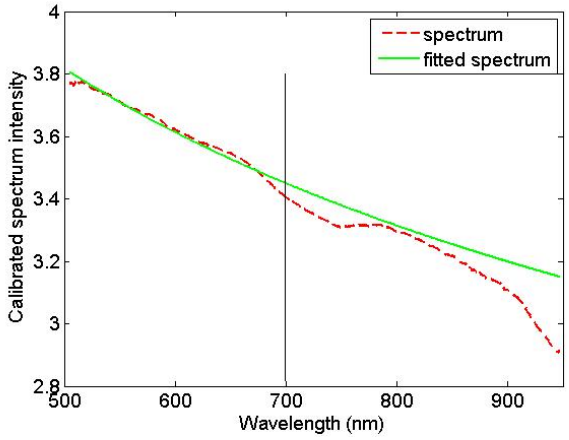

Fig. 4.8 Reflectance spectrum of 20% Intralipid and its empirical power law fit

When considering power law fits to scattering spectrum, there are two parameters within the fitted equation that represent the scattering properties. Parameter *A* is the scattering amplitude, which represents the scattering intensity. And parameter *b* is the scattering power, which represents how scattering coefficient changes as the wavelength changes. And in Fig. 4.9 and Fig. 4.10, the scattering amplitude *A* (red *) and scattering power *b* versus the reduced scattering coefficient of Intralipid are shown, respectively. The scattering coefficients are calculated using Eqn (4.1) from the concentration of Intralipid.

In Fig. 4.9, the linear relationship between the scattering amplitude and the reduced scattering is maintained, since the scattering amplitude is representative of the spectrum intensity.

According to Mie scattering theory, the scattering power is supposed to be constant for Intralipid with different concentrations since the particle properties are the same except the particle density. However, instead of a straight line, we notice that the scattering power obtained from Intralipid fluctuated from 0.3 to about 0.5 as the reduced scattering coefficients change, or the concentrations change. However, this fluctuation is expected due to the instability of the system and the shape of scattering spectrum is more prone to noises than the intensity.

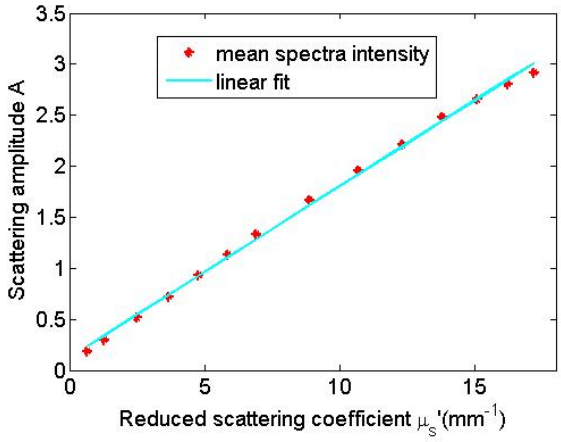

Fig. 4.9 Scattering amplitude of Intralipid vs. its reduced scattering coefficient

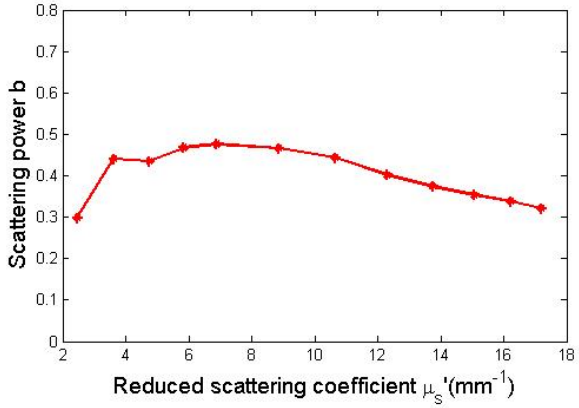

Fig. 4.10 Scattering power of Intralipid vs. its reduced scattering coefficient

4.2.3 Absorption spectrum of Intralipid

As shown in Fig. 4.8, the reflectance spectrum disperses from the fitted power law curve after 700nm, which is the evidence of the existence of absorption. Since calibrated spectrum is modeled as the product of the scattering spectrum and absorption spectrum, the absorption spectrum could be obtained by dividing the calibrated spectrum by the scattering spectrum, as:

$$R_{abs} = \frac{R_{ref}}{R_s} = \frac{R_s * R_{abs}}{R_s} \tag{4.5}$$

where R_s is the scattering spectrum of Intralipid, which is calculated by using power law equation to fit the reflectance spectrum from 500 to 700nm. For example, the absorption spectrum of 20% Intralipid is obtained by dividing the red dash line by the green solid line in Fig. 4.8. Fig. 4.11 shows the resulted absorption spectrum of 20% Intralipid (red solid line) and its theoretical absorption spectrum.

The theoretical absorption spectrum is modeled by Lambert-beer's Law, as shown

$$R_{abs\_simu} = e^{-u_a L} = \mathrm{e}^{-(u_{a\_water} * (1-c) + u_{a\_lipid} * c) * \frac{1.34 d e^{0.17 d}}{(u_s' d)^{0.23} (0.52 + (u_a d)^{0.52})}} \tag{4.6}$$

The absorption coefficients of Intralipid is calculated by Eqn (4.2), and for 20% Intralipid, c = 0.2. The path length L is calculated by Eqn (3.9) with the diameter of fiber to be d = *0.32mm*. The path length is a function of both absorption coefficient and reduced scattering coefficient. The theoretic reduced scattering coefficient is calculated by Mie theory.

We could see a very good correlation between the measured absorption spectrum and the theoretical absorption spectrum, as shown in Fig. 4.11.

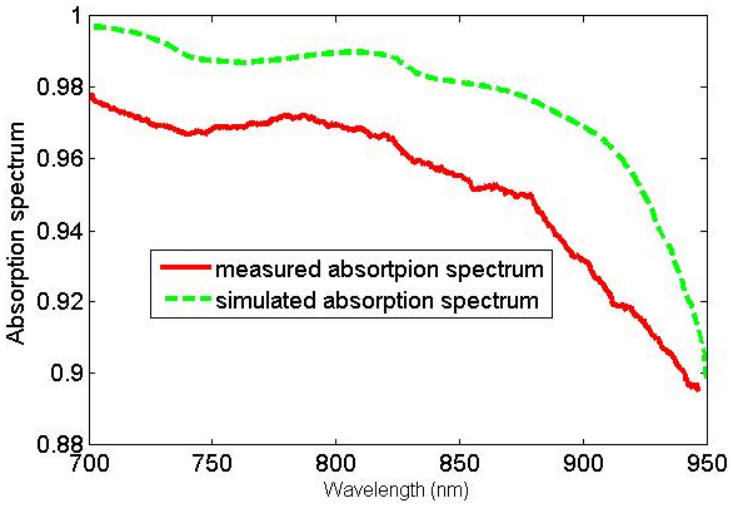

Fig. 4.11 Measured absorption spectrum and theoretical absorption spectrum of 20% Intralipid

4.3 Polystyrene phantom study

Polystyrene phantoms (Phosphorex, Inc. Fall River, MA, USA) are 5 ml nanospheres polystyrene solutions with different mean particle sizes. And the solid concentrations within the polystyrene phantoms are all 1%. The distribution of the particle size is assumed to be Gaussian distribution but with different standard derivation. Three polystyrene phantoms with mean particle size to be 99nm, 206.5nm, and 500nm were used for our study. And the standard derivations of these three polystyrene phantoms are 11nm, 20.6nm and 12nm, respectively. In Fig. 4.12 the particle size distribution histograms of the polystyrene phantoms are shown.

The theoretical reduced scattering coefficients of the polystyrene phantoms are calculated using Mie scattering theory, as shown in Fig. 4.13. The measured reflectance spectra using our single fiber reflectance spectroscopy configuration of these three phantoms are shown in Fig. 4.14. In Fig. 4.13 and Fig. 4.14, the intensities of the spectra are normalized at 500nm. Comparing the theoretical reduced scattering coefficient spectra in Fig. 4.13 and the reflectance spectra in Fig. 4.14, we observe that the shape changes of the measured reflectance spectra follow that of the theoretical reduced scattering coefficient spectra, which further confirms the reflectance spectrum

of single fiber reflectance spectroscopy does linear to the reduced scattering coefficient of the medium.

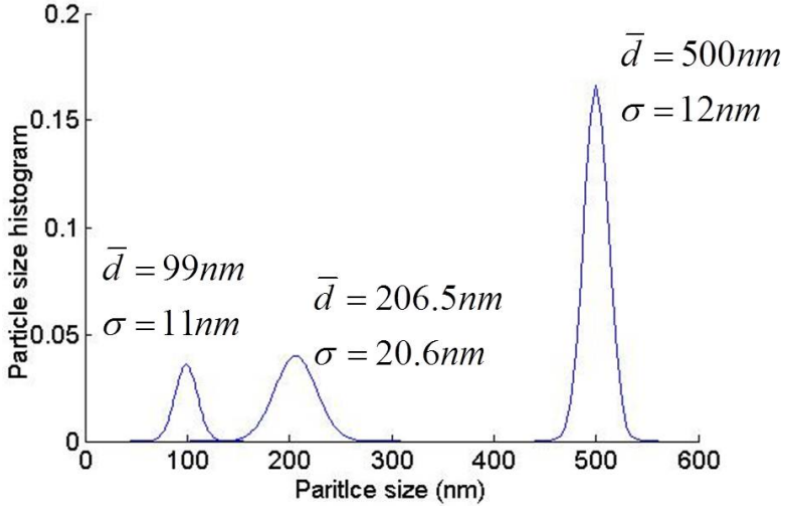

Fig. 4.12 Particle size histograms of polystyrene phantoms

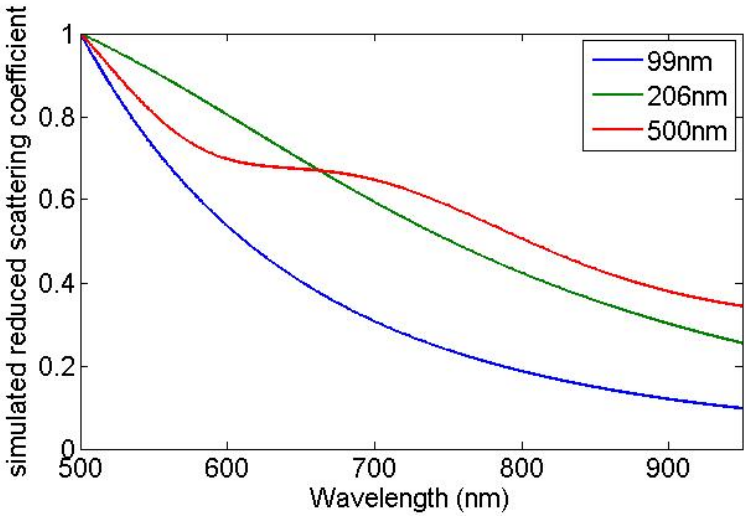

Fig.4.13 Theoretical reduced scattering coefficients of polystyrene phantoms

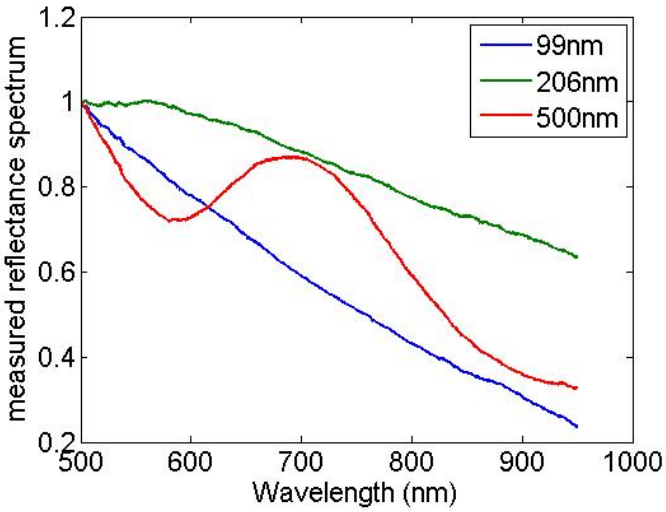

Fig. 4.14 Measured reflectance spectra of polystyrene phantoms

CHAPTER V

CADAVER STUDIES

The single-fiber optical reflectance spectroscopy system is compatible to and readily integratable in the PLDA procedure. In this chapter, the single fiber reflectance spectroscopy system is employed on cadaver discs *in situ* to evaluate the spectra differences before and after PLDA procedure, and between normal and calcified discs. The operation procedures on cadaver discs are introduced and the results are shown and discussed.

5.1 Imaging protocol and cadaver samples

The imaging protocol on canine species has been approved by the Institutional Animal Care and Use Committee (IACUC) of Oklahoma State University. For this study, however, only cadaveric dogs were used for testing to discover the relationship between the changes of tissue reflection spectra and the expected changes of disc tissue contents. The discs being evaluated include T (Thoracic) 8-9 to L (Lumber) 5-6. Before performing any tests, the discs were examined by radiography to locate any possible calcified discs. twenty gauge myelographic spinal needles were inserted through the paralumbar muscles and the fibrosus annulus and positioned in the middle of nucleus pulposus in the intervertebral discs under investigation using fluoroscopic guidance, as show in Fig. 5.1 After retracting the stylet of the spinal needle, the fiber sensor was introduced into the nuclues of the disc, as shown in Fig. 5.2, and was consistently positioned approximately 1mm distal to the tip of the spinal needle using fiber cladding trimmed to the appropriate length. For each disc, a total of 5 repeated spectral measurements were taken at integration time of two seconds per measurement, a time scale that is limited by the weak illumination of the compact tungsten light source. After preoperative measurements, 40 seconds

of PLDA laser ablation procedure was performed on most discs using a 2W Ho:YAG. Post-ablation reflectance spectra were then measured following the same procedure as preoperative measuremts. The measurments from pre-oeprative and post-operative discs were compared against those from air and water for calibration. The total time necessary for spectral data collection for 10 discs adds approximately 10 minutes to the overall PLDA procedure. The measured spectra were displayed in realtime and stored automatically, but the analysis of data was performed off-line.

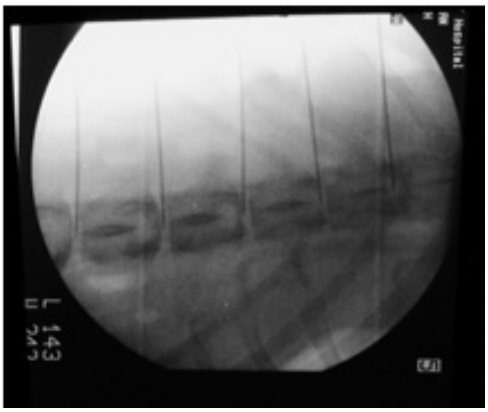

Fig. 5.1 The position of needle in the disc (nucleus pulposus) is confirmed by fluoroscopy.

Fig. 5.2. Procedure of inserting the optical fiber into the intervertebral disc via twenty gauge spinal needle

Six cadeveric canines were tested. Among them four dogs were nonchondrodystrophoid breeds and two were chondrodystrophoid breeds. The summary of discs data collected from the six canine cadaver spcimens were shown in Table.5.1.

Table 5.1 Summary of disc data collected from canine cadaver specimens.

Canine Cadaver ID	Dog breed	Mineralized Discs on Radiographs	Spectroscopy Performed (pre and post ablation)	Laser Ablated Discs
M	nonchondrodystrophoid	L2-3, L3-4 (possibly)	T10-11, T11-12, T13-L1 thru L5-6	T13-L1 thru L3-4
Q	nonchondrodystrophoid	none	T7-8, T9-10 thru L5-6	T10-11 thru L3-4
Y	nonchondrodystrophoid	none	T8-9, T10-11 thru L5-6	T10-11 thru L4-5
Z	nonchondrodystrophoid	none	T12-13, L1-2, L3-4 thru L5-6	T12-13, L1-2, L3-4, L4-5
A	chondrodystrophoid	T9-10, T10-11, T11-12, L3-L4	T8-9 thru L5-6	T8-9 thru L5-6
B	chondrodystrophoid	T11-12	T9-10 thru L5-6	T9-10 thru L5-6

As discussed in Chapter 2, the nonchondrodystrophoid discs do not undergo degeneration easily. Radiagraphs illustrates that only discs L2-3 and L3-4 in dog M were possibly slightly mineralized. However, data from the nonchondrodystrophoid dogs were important for analysing the reflectance spectrum of discs and to compare the pre and post ablation disc spectrum. Dog A is a dachshund, a breed that is very prone to intervertebral degeneration. Radiagraphs showed that four discs, T9-10, T10-11, T11-12 and L3-L4 were fully calcified. Dog B is also chonndrodystrophoid breed with disc T11-12 confirmed to be calcified. Two rounds of the spectra measurements were done on Dog A and Dog B both before and after disc ablation to validate the repeatablity of the results. During disc ablation, 60 seconds of ablation was applied to the discs that are believed to be calcified instead of conventional 40 seconds.

5.2 Results

5.2.1 Nonchondrodystrophoid disc spectrum

From the preliminary tests on nonchondrodystrophoid canine cadaveric intervertebral discs *in situ*, changes of reflectance spectra prior to and after disc laser ablation were observed. The reflectance spectra were calibrated using Eqn (3.2). The average spectra acquired prior to PLDA (red solid line) and after PLDA (green dash line) of the four dogs are compared in Figs. 5.3-5.6. The vertical bars in the figures show the spectrum standard derivation between different discs. The spectra are shown from 550nm to 950 nm because there are significant artifacts at lower than 550nm range. The common features of the four measurements are that the post-PLDA spectra are wavelength-independent in the range of 650-950nm, whereas the pre-PLDA spectra are all similar to the Intralipid spectra in terms of the decreasing trend as the wavelength increases, which indicates a scattering dominant medium. For three out of four dogs, the average reflectance spectra of post-PLDA measurement are lower than that of pre-PLDA measurements in spectral range below 800nm, however, the data have significant variance. Nevertheless, the flatness and the intensity reduction of the post-PLDA spectra agree with the PLDA process that destroyed the tissue cellular structures and removed the scattering particles.

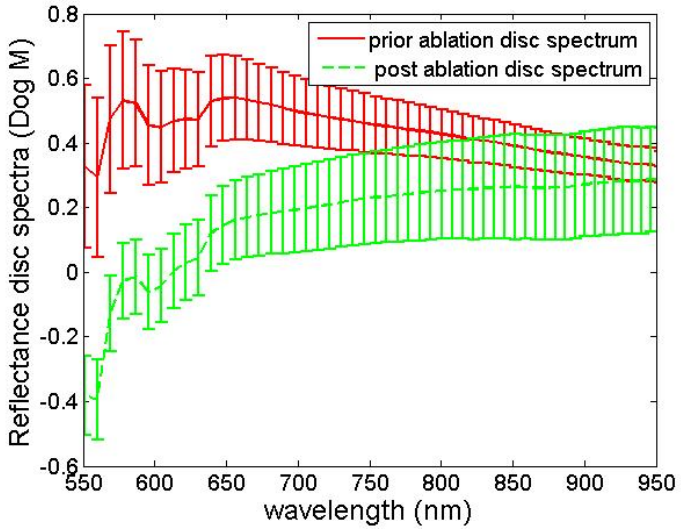

Fig. 5.3 Prior and post ablatoin spectra of discs in Dog M

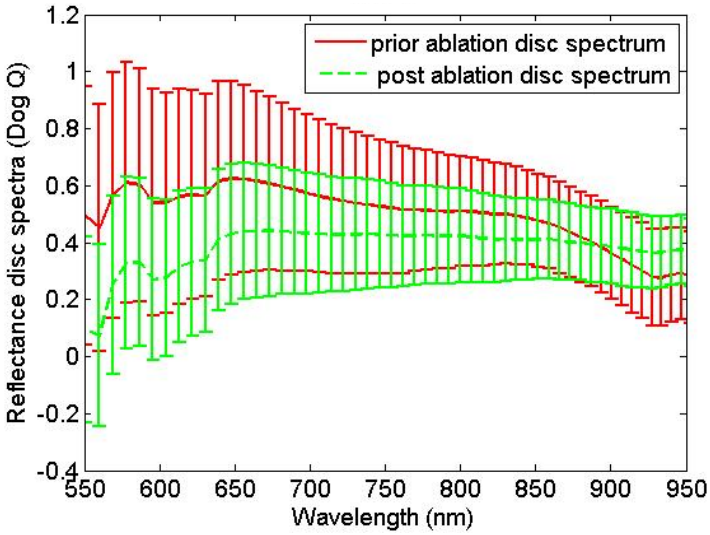

Fig. 5.4 Prior and post ablatoin spectra of discs in Dog Q

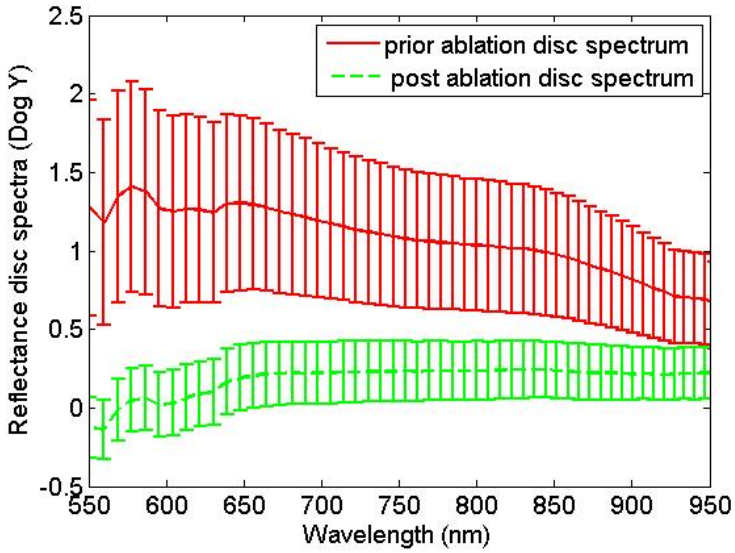

Fig. 5.5 Prior and post ablatoin spectra of discs in Dog Y

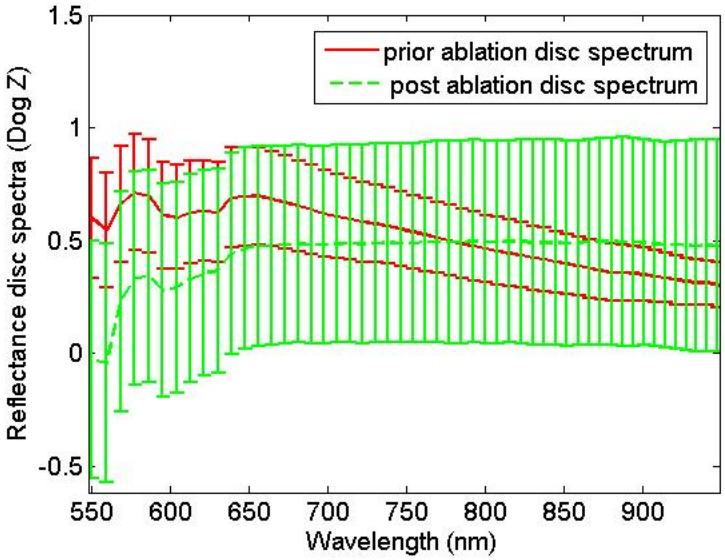

Fig. 5.6 Prior and post ablatoin spectra of discs in Dog Z

The average spectra of normal discs (red solid line) and calcified discs (green dash line) of Dog M are also compared in Fig. 5.7. We could see that the average spectrum intensity of degenerated discs is slightly higher than that of normal discs. However, no clear cutoff is observed due to

small intensity differences between normal and calcified discs compared to the large variance of normal disc spectrum intensity.

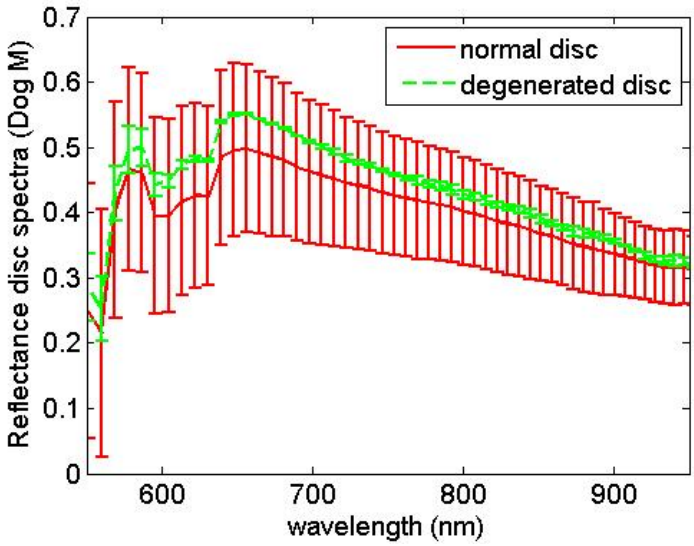

Fig. 5.7 Comparison of normal and calcified discs' spectra in Dog M

5.2.2 Modified Model for disc spectrum

When applying the single fiber reflectance spectrum spectroscopy system in the nucleus pulposus of canine intervertebral disc, we assume that the surrounding tissues have no influence on the reflectance spectrum. However, the surrounding tissues, and the tissues through which the needle has passed can contaminate the reflectance spectrum. Considering these, the measured spectrum of cadaveric disc should be modified from Eqn (3.3) to

$$R_{disc}(\lambda) = \eta(\lambda)[au'_s(\lambda)e^{-u_a(\lambda)L}\varphi(\lambda) + \eta_{samplefiber}\varphi(\lambda) + \gamma(\lambda)\times\varphi_s(\lambda) + R_s(\lambda)] \quad (5.1)$$

Comparing Eqn (5.1) to Eqn (3.3), there is an addition term $R_s(\lambda)$ in Eqn (5.1), which is the reflectance spectrum of the surrounding tissues and other possible contaminations.

When applying calibration procedure, the calibrated spectrum of intervertebral disc is modeled as

$$
\begin{aligned}
R(\lambda) &= \frac{R_{disc}(\lambda) - R_{water}(\lambda)}{R_{air}(\lambda) - R_{water}(\lambda)} \\
&= \frac{\eta(\lambda)[(au'_s(\lambda))e^{-u_a(\lambda)L}\varphi(\lambda) + \eta_{samplefiber}\varphi(\lambda) + \gamma(\lambda)\times\varphi_s(\lambda) + R_s(\lambda) - \eta_{waterfiber}\varphi(\lambda) + \gamma(\lambda)\times\varphi_s(\lambda)]}{\eta(\lambda)[\eta_{airfiber}\varphi(\lambda) + \gamma(\lambda)\times\varphi_s(\lambda)] - \eta(\lambda)[\eta_{waterfiber}\varphi(\lambda) + \gamma(\lambda)\times\varphi_s(\lambda)]} \\
&= \frac{(au'_s(\lambda))e^{-u_a(\lambda)L} + \eta_{samplefiber} - \eta_{waterfiber} + R_s(\lambda)/\varphi(\lambda)}{\eta_{airfiber} - \eta_{waterfiber}} \\
&= \alpha u_s'(\lambda)e^{-u_a(\lambda)L} + \beta + \omega\gamma_s(\lambda)
\end{aligned}
\tag{5.2}
$$

where $\gamma_s(\lambda) = R_s(\lambda)/\varphi(\lambda)$ and ω is a constant.

And we could see the calibrated spectrum contains an extra wavelength dependent term $\omega\gamma_s(\lambda)$.

Similarly, the contaminant reflectance exists in post ablation disc spectrum, too. Although the discs' nucleus pulposus becomes a non-scattering medium after ablation, reflectance scattering comes from the contaminate tissues could still be detected by the spectrometer. We assume that the scattering reflectance spectrum from the contaminate tissues in the post ablation discs is the same as that in prior ablation discs. The measured spectrum of post ablation cadaver disc should be modeled as

$$
R_{post\_disc}(\lambda) = \eta(\lambda)[\eta_{discfiber}\varphi(\lambda) + \eta_{samplefiber}\varphi(\lambda) + \gamma(\lambda)\times\varphi_s(\lambda) + R_s(\lambda)] \tag{5.3}
$$

After applying calibration procedure,

$$
\begin{aligned}
R_{post}(\lambda) &= \frac{R_{post\_disc}(\lambda) - R_{water}(\lambda)}{R_{air}(\lambda) - R_{water}(\lambda)} \\
&= \frac{\eta(\lambda)[\eta_{discfiber}\varphi(\lambda) + \eta_{samplefiber}\varphi(\lambda) + \gamma(\lambda)\times\varphi_s(\lambda) + R_s(\lambda) - \eta_{waterfiber}\varphi(\lambda) + \gamma(\lambda)\times\varphi_s(\lambda)]}{\eta(\lambda)[\eta_{airfiber}\varphi(\lambda) + \gamma(\lambda)\times\varphi_s(\lambda) - \eta_{waterfiber}\varphi(\lambda) + \gamma(\lambda)\times\varphi_s(\lambda)]} \\
&= \frac{\eta_{discfiber} + \eta_{samplefiber} - \eta_{waterfiber} + R_s(\lambda)/\varphi(\lambda)}{\eta_{airfiber} - \eta_{waterfiber}} \\
&= \alpha_1 + \omega\gamma_s(\lambda)
\end{aligned}
\tag{5.4}
$$

We could see the calibrated spectrum of post ablation disc contains the same wavelength dependent term $\omega\gamma_s(\lambda)$.

Subtracting Eqn (5.4) from Eqn (5.2), we could get

$$R(\lambda) = R_{pre} - R_{post} = \alpha\mu_s'(\lambda)e^{-\mu_a(\lambda)L} + \beta + \omega\gamma_s(\lambda) - \alpha_1 - \omega\gamma_s(\lambda) = \alpha\mu_s'(\lambda)e^{-\mu_a(\lambda)L} + \beta \quad (5.5)$$

We could see that modified reflectance spectrum regains the linear relationship with the reduced scattering coefficient of the nucleus pulposus.

In Fig. 5.7, the modified disc spectrum of Dog Y (blue dot line) is shown. For comparison, the original calibrated pre-ablation (red solid line) and post ablation (green dash line) disc spectra are also shown in Fig. 5.8. We could see that after applying modified calibration algorithm, the artifacts at the lower wavelength range are reduced and the spectrum shows a more clearly exponentially decreasing trend as expected. Similar results could also be observed in Dog M, Q and Z but only Dog Y's results are shown here.

Fig. 5.9 shows the empirical power law fit to the modified reflectance spectrum of Dog Y within 500 to 700nm range, where the absorption of water is extremely low. We could see that the modified disc spectrum follows exponentially decay trends precisely, as the model indicated. However, at higher wavelength range, the modified reflectance spectrum of the disc is tapered down from the fitted scattering spectrum due to the absorption of water.

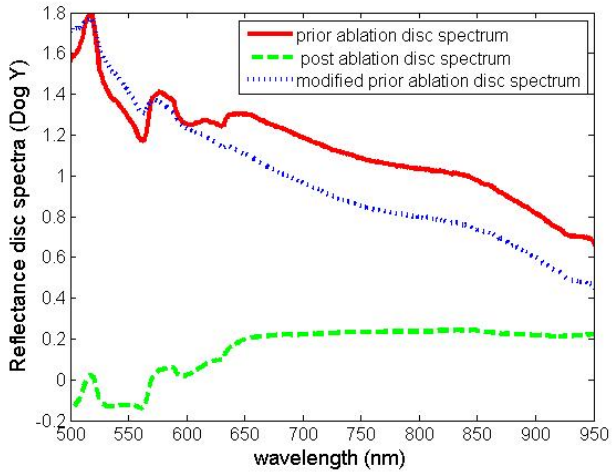

Fig. 5.8 Modified reflectance spectrum of cadaveric disc in Dog Y

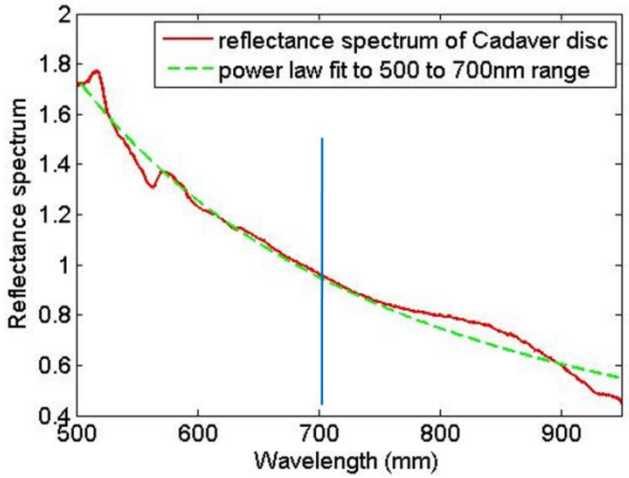

Fig. 5.9 Empirical power law fit to modified reflectance spectrum of Dog Y

5.2.3 Chondrodystrophoid disc spectrum

Spectrum differences between normal discs and calcified discs are observed even from the original measured spectra in chondrodystrophoid dogs. One of original disc spectra is shown in Fig. 5.10. The spectrum peak intensities at around 730nm of different discs in Dog A and Dog B are shown in Fig. 5.11. The peak intensity is calculated by averaging the spectrum intensity within 720nm and 745nm (the red square in Fig. 5.10). In Fig. 5.11, the cyan square marks show the peak intensity of normal discs in Dog A from round 1 test, the cyan circle marks show the value of normal discs in Dog A form round 2 tests, the red diamond marks represent the result of calcified discs in Dog A from round 1 tests, the red star marks indicate the results of calcified discs in Dog A from round 2 tests**,** the blue up triangle marks show the peak intensity of normal discs in Dog B from round 1 test, the blue down triangle marks show the value of normal discs in Dog B form round 2 tests, the magenta x-marks represent the result of calcified discs in Dog B from round 1 tests, and the magenta plus marks indicate the results of calcified discs in Dog B from round 2 tests**.** And we could see the peak intensity of calcified discs is higher than that of the normal discs in both rounds of tests for both Dog A and Dog B. However, the overall peak intensity of Dog B seems to be lower than that of Dog A, which is caused by lower source

intensity output at time of measuring in Dog B. We also observe that the spectrum intensity is different for the same discs at different sets of tests. This could be caused by the instability of the source output or the different sensing spot, or both. Furthermore, we observed that for Dog A, the closer a normal disc to the mineralized disc, the higher the intensity of the spectrum. Or, the farther a normal disc from the mineralized disc, the lower the intensity reading of the spectrum. This may indicate that discs close to mineralized discs are undergoing mild degenerations that are not detected by radiography. The spectrum intensity may correlate with the degree of degeneration.

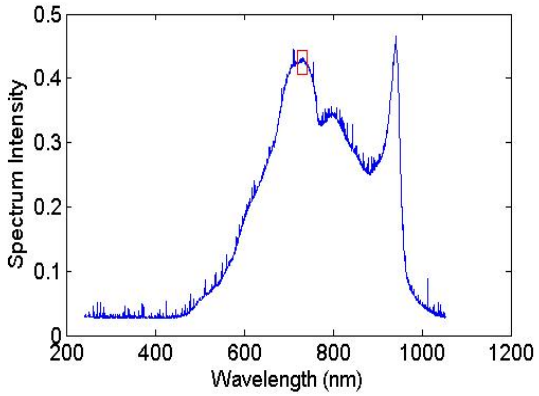

Fig. 5.10 Original reflectance spectrum of cadaveric disc

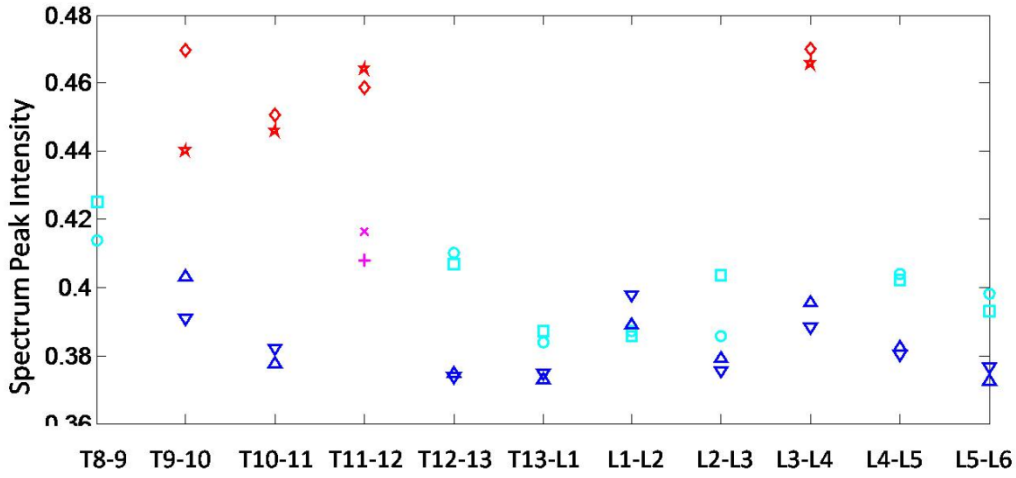

Fig. 5.11 Peak spectrum intensity of cadaveric discs in Dog A & B

The differences between normal and calcified disc spectra could be observed more clearly from calibrated spectra, as shown in Fig. 5.12. The red dot line shows the average calibrated spectrum of normal discs and the green solid line shows the average calibrated spectrum of calcified discs. The error bars represent the standard derivation between different measurements.

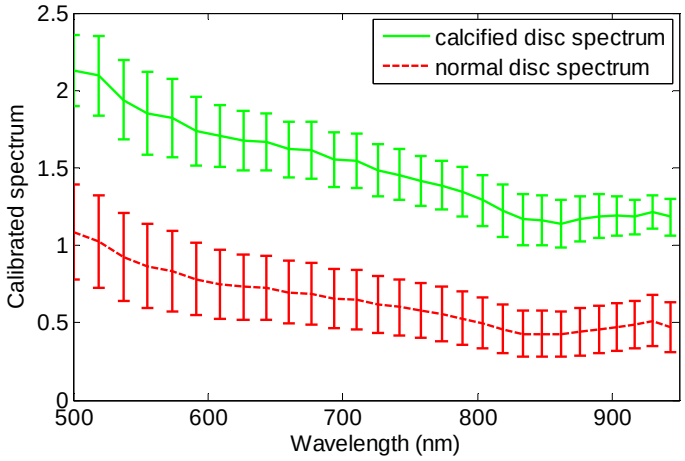

Fig. 5.12 Comparison between calcified and normal disc spectra

The spectrum differences between the normal and calcified discs are further analyzed by the fitted scattering amplitude *A* and scattering power *b*, which are shown in Fig. 5.13 and Fig. 5.14, respectively. The power law fitting was applied to spectrum range between 500nm to 950nm. In Fig. 5.13 and Fig. 5.14, the cyan square marks show the peak intensity of normal discs in Dog A from round 1 test, the cyan circle marks show the values of normal discs in Dog A form round 2 tests, the red diamond marks represent the results of calcified discs in Dog A from round 1 tests, the red star marks indicate the results of calcified discs in Dog A from round 2 tests**,** the blue up triangle marks show the peak intensity of normal discs in Dog B from round 1 test, the blue down triangle marks show the values of normal discs in Dog B form round 2 tests, the magenta x-marks represent the results of calcified discs in Dog B from round 1 tests, and the magenta plus marks indicate the results of calcified discs in Dog B from round 2 tests**.**

We could see that for calcified discs, the scattering amplitude *A* is higher while the scattering power *b* is lower. The scattering property changes of nucleus pulposus revealed by the reflectance spectrum are supposed to be related to its microstructure changes. As seen in Fig. 5.13, the scattering amplitude of normal discs is lower than that of calcified discs, which could be explained by the fact that the calcification within the disc increases scattering density within the disc. Moreover, the calcification within the disc is supposed to have larger diameter than normal cell organelle, which correlates to the fact that the scattering power is lower in the calcified disc, as shown in Fig. 5.14.

The difference in the overall spectrum intensity between Dog A and Dog B that has been observed in Fig. 5.11 doesn't exist in the overall intensity of scattering amplitude and scattering power, as shown in Fig. 5.13 and Fig. 5.14, which means the calibrating procedure eliminate the influence of source intensity instability to some extent.

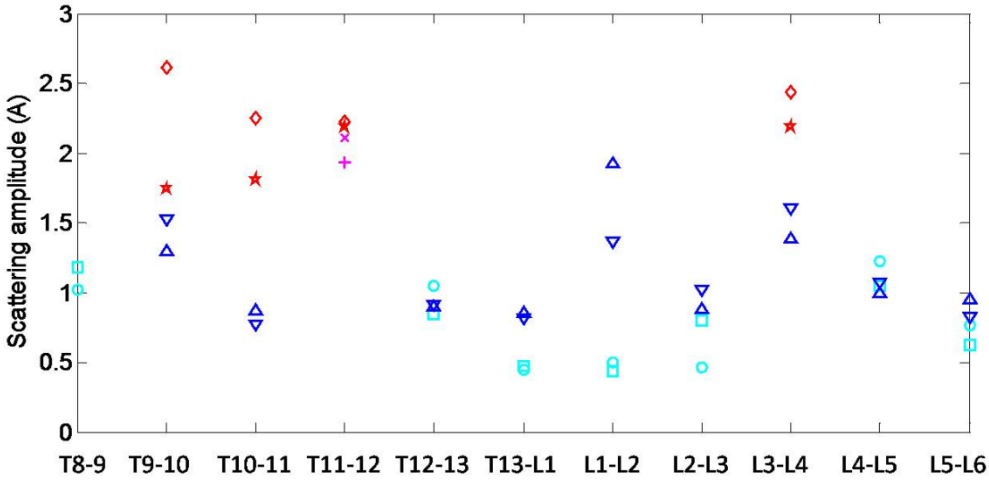

Fig. 5.13 Scattering amplitude of the calibrated discs' spectra in Dog A & B

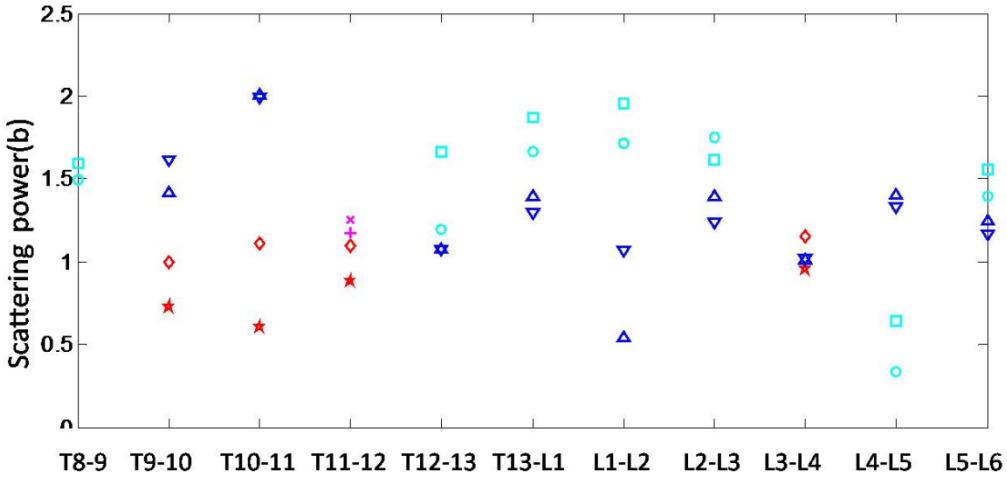

Fig. 5.14 Scattering power of the calibrated discs' spectra in Dog A & B

Fig. 5.15 shows the Receiving Operating Characteristic (ROC) curves when using the scattering power, scattering amplitude and the peak intensity of the original spectrum to classify the discs. ROC curve is a graphical plot of the sensitivity, or true positive rate vs. the specificity, or the false positive rate for a classifier system as its discrimination threshold is varied. The sensitivity is defined as

$$sensitivity = \frac{number\ of\ true\ positive\ result}{number\ of\ true\ positive\ result + number\ of\ \ false\ negative\ result} \tag{5.6}$$

And the specificity is defined as

$$specificity = \frac{number\ of\ true\ negative\ result}{number\ of\ \ false\ positive\ result + number\ of\ true\ negative\ result} \tag{5.7}$$

In ROC space, a diagonal line from the left bottom to the top right corners (shown as the purple dash line in Fig. 5.15) defines a random guess with 50% accuracy. And points above the diagonal represent good classification results with the best classification point at the left up corner (0, 1).

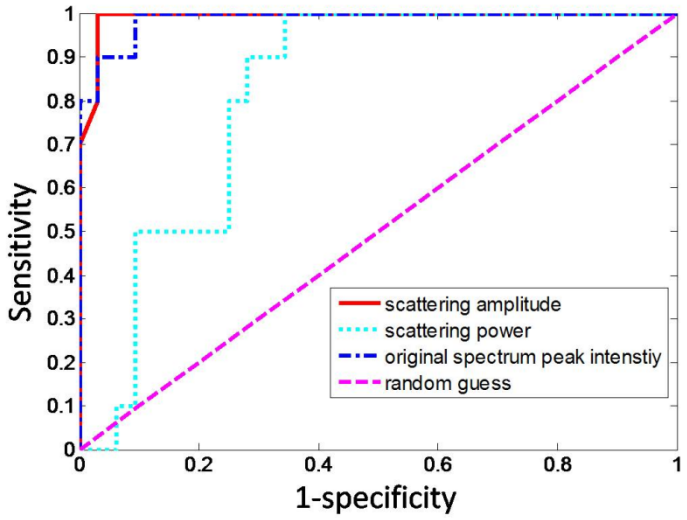

Fig. 5.15 ROC curves when using scattering power, scattering amplitude and original spectrum peak intensity to differentiate normal and calcified discs

We could see a significant good ROC curve when using scattering amplitude to differentiate the normal and calcified discs with the area under curve to be 99.22%. When using the original spectrum peak intensity to distinguish the normal and calcified discs, the area under curve is calculated to be 98.75%. Although less accurate, 82.19% of area under curve is achieved by using scattering power as a classifier.

After disc ablation, the masses within the nucleus are expected to be ablated, and the discs become non-scattering media. As observed in the nonchondrodystrophoid discs, the post ablation disc spectra are relatively low and flat than the pre ablation disc spectra.

CHAPTER VI

CONCLUSION AND DISCUSSION

6.1 Conclusion

Extrusion or protrusion of an intervertebral disc is a common, frequently debilitating, painful, and sometimes fatal neurologic disease in the chondrodystrophic dog. This work proposed using the fiber-needle based sensing configuration for evaluating the changes in canine intervertebral disc in response to laser disc ablation, directed towards detecting the mineralization and water loss within the nucleus pulposus of the intervertebral disc due to degeneration.

This work built a single fiber reflectance spectroscopy system and proposed the calibration method and model. The calibrated spectrum is modeled as to be linear to the reduced scattering coefficient of the medium and be attenuated by absorption. However, a linear relationship between the reflectance spectrum and its reduced scattering coefficient is expected when the absorption is neglected, which has been validated by Intralipid phantoms with different concentrations. Furthermore, Intralipid studies show that two parameters, scattering amplitude and scattering power, are representative to the reflectance spectrum of single fiber reflectance spectroscopy in terms of its intensity and its shape.

Cadaver studies have been performed on four nonchondrodystrophoid dogs and two chondrodystrophoid dogs. Preliminary studies on nonchondrodystrophoid dogs indicate that the reflectance spectrum of pre ablation disc shows higher intensity and follows the exponentially

decreasing trend as expected from a scattering medium. However, post ablation disc spectrum is flattened, which confirms a less scattering medium within the nucleus after ablation. Reflectance spectrum differences between normal and calcified discs have been observed in chondrodystrophoid dogs. The hypothesis that calcified discs nucleus pulposus represents a higher scattering medium is validated by the fact that the intensity of normal disc spectral is lower than that of the calcified disc. The higher scattering amplitude but lower scattering power within calcified discs also reveals that the higher scattering in calcified disc comes from higher scatter density and larger scatter particle size. The ROC curve drawn from limited data using scattering amplitude as a classifier shows that the scattering amplitude has 99.22% area under curve.

Although the absorption is low in this study, the water absorption still shows its footprint in the reflectance spectrum. However, due to the large spectrum noises and the small changes caused by water absorption, the water content changes in the disc haven't been observed from the reflectance spectrum.

Therefore, this fiber-needle based sensing configuration may be feasible for integrating the evaluation of calcification and water content into the clinical procedure of Ho:YAG laser disc ablation for pre-operative real-time detection and post-operative evaluation of therapeutic interventions regarding the chondrodystrophic disc.

6.2 Future work

The current work is a preliminary study which investigates the feasibility of using single fiber reflectance spectroscopy system to sense the intervertebral changes caused by disc degeneration and disc ablation. However, in order to quantitatively diagnose disc degeneration, more work still needs to be done.

The reflectance spectroscopy system could give a more stable output by several upgrades. Due to the instability of the source, there are large variances on detected signals, which might be solved

by adding another channel for source intensity monitor or using source detector cooling techniques. By doing these, the water content changes within the discs may be detected. And also the accuracy of scattering power could be improved.

We have observed that the spectrum intensity of the normal disc near the calcified disc is higher than those more distant, which may indicate that the disc near the calcified disc is slightly degenerated. When relate the spectrum intensity with the histological characteristics of the nucleus pulposus, such as the average Hounsfield Unit within the nucleus pulposus from CT, a quantitative degree of degeneration might be determined by this method.

Furthermore, the current ROC curves are drawn based on limited data, more samples are essential for smoother ROC curves.

The reflectance spectrum has the potential to quantitatively determine the microstructure changes within the disc. We have related the higher scattering amplitude and lower scattering power in calcified disc to higher scatter density and larger scatter diameter. But to quantitatively determine the microstructure changes within the nucleus pulposus, intensive studied are to be performed to calibrate the relationship between the reflectance spectrum changes and the microstructure changes.

And finally, *in vivo* test on canine patients is desired to validate the results already obtained.

REFERENCES

[1] Bartels, K.E., et al., *Outcome of and complications associated with prophylactic percutaneous laser disk ablation in dogs with thoracolumbar disk disease: 277 cases (1992-2001).* J Am Vet Med Assoc, 2003. 222(12830867): p. 1733-1739.

[2] Stigen, Ø. and Ø. Kolbjørnsen, *Calcification of intervertebral discs in the dachshund: a radiographic and histopathologic study of 20 dogs.* Acta Veterinaria Scandinavica, 2007. 49(1): p. 1-7.

[3] Matcher, S.J., Winlove, C.P., and Gangnus, S.V., *The collagen structure of bovine intervertebral disc studied using polarization-sensitive optical coherence tomography.* Phys Med Biol, 2004. 49(15128206): p. 1295-1306.

[4] Robert, L.P.v.V. and et al., *Optical biopsy of breast tissue using differential path-length spectroscopy.* Physics in Medicine and Biology, 2005. 50(11): p. 2573.

[5] Bard, M.P.L., et al., *Measurement of Hypoxia-related Parameters in Bronchial Mucosa by Use of Optical Spectroscopy.* Am. J. Respir. Crit. Care Med., 2005. 171(10): p. 1178-1184.

[6] Amelink, A., et al., *Non-invasive measurement of the morphology and physiology of oral mucosa by use of optical spectroscopy.* Oral Oncol, 2008. 44(17350324): p. 65-71.

[7] Zonios, G., Bykowski, J., and Kollias, N., *Skin melanin, hemoglobin, and light scattering properties can be quantitatively assessed in vivo using diffuse reflectance spectroscopy.* J Invest Dermatol, 2001. 117(11886508): p. 1452-1457.

[8] Chen, S.S., et al., *Measurement of redox states of mitochondrial cytochrome aa3 in regions of liver lobule by reflectance microspectroscopy.* Am J Physiol, 1993. 264(8383443): p. 375-382.

[9] Koenig, F., et al., *Spectroscopic measurement of diffuse reflectance for enhanced detection of bladder carcinoma.* Urology, 1998. 51(2): p. 342-345.

[10] Reif, R., A'Amar, O., and Bigio, I.J., *Analytical model of light reflectance for extraction of the optical properties in small volumes of turbid media.* Appl Opt, 2007. 46(17932546): p. 7317-7328.

[11] Bigio, I.J. and Bown, S.G., *Spectroscopic sensing of cancer and cancer therapy: Current status of translational research.* Cancer Biol. Ther., 2004. 3(3): p. 259-267.

[12] Dehghani, H., et al., *Multiwavelength three-Dimensional Near-Infrared tomography of the breast: initial simulation, phantom, and clinical results.* Appl. Opt., 2003. 42(1): p. 135-145.

[13] Piao, D., et al., *Alternative Transrectal Prostate Imaging: A Diffuse Optical Tomography Method.* Selected Topics in Quantum Electronics, IEEE Journal of, 2010. 16(4): p. 715-729.
[14] Kanick, S.C., Sterenborg, H.J.C.M., and Amelink, A., *Empirical model of the photon path length for a single fiber reflectancespectroscopy device.* Opt. Express, 2009. 17(2): p. 860-871.
[15] Mourant, J.R., et al., *Spectroscopic diagnosis of bladder cancer with elastic light scattering.* Lasers in Surgery and Medicine, 1995. 17(4): p. 350-357.
[16] Vo-Dinh, T., et al., *In vivo cancer diagnosis of the esophagus using differential normalized fluorescence (DNF) indices.* Lasers in Surgery and Medicine, 1995. 16(1): p. 41-47.
[17] Kanick, S.C. and et al., *Monte Carlo analysis of single fiber reflectance spectroscopy: photon path length and sampling depth.* Physics in Medicine and Biology, 2009. 54(22): p. 6991.
[18] Kanick, S.C., et al., *Integration of single-fiber reflectance spectroscopy into ultrasound-guided endoscopic lung cancer staging of mediastinal lymph nodes.* Journal of Biomedical Optics, 2010. 15(1): p. 017004-8.
[19] Fabbri, F., Franceschini, M.A., and Fantini, S., *Characterization of Spatial and Temporal Variations in the Optical Properties of Tissuelike Media with Diffuse Reflectance Imaging.* Appl. Opt., 2003. 42(16): p. 3063-3072.
[20] Prahl, S. *Optical absorption of water*. Available from: http://omlc.ogi.edu/spectra/water/index.html.
[21] Prahl, S. *Optical absorption of hemoglobin.* Available from: http://omlc.ogi.edu/spectra/hemoglobin/.
[22] Luttgen, P.J. *Canine intervertebral disk disease*. Available from: http://www.dachshund-dca.org/discbook.html.
[23] Kroll, E. *FCE fibrocartilaginous emboli*. Available from: http://www.wolfhouse.dk/articles/fce.php.
[24] Dang, L., Wardlaw, D., and Hukins, D., *Removal of nucleus pulposus from the intervertebral disc – the use of chymopapain enhances mechanical removal with rongeurs: a laboratory study.* BMC Musculoskeletal Disorders, 2007. 8(1): p. 1-4.
[25] Coventry, M.B., *Anatomy of the intervertebral disk.* Clin. Orthop. Relat. Res., 1969. 67: p. 9-15.
[26] Bray, J.P. and Burbidge, H.M., *The canine intervertebral disk: part one: structure and function.* J Am Anim Hosp Assoc, 1998. 34(9527431): p. 55-63.
[27] Marchand, F. and Ahmed, A.M., *Investigation of the laminate structure of lumbar disc anulus fibrosus.* Spine (Phila Pa 1976), 1990. 15(2363068): p. 402-410.
[28] Hansen, H.J., *A pathologic-anatomical study on disc degeneration in dog, with special reference to the so-called enchondrosis intervertebralis.* Acta. Orthop. Scand. Suppl., 1952. 11: p. 1-117.
[29] Evans, H.E. and Christensen, G.C., *Miller's anatomy of the dog*. 2nd ed. 1979, Philadelphia: WB Saunders.
[30] Hendry, N.G.C., *The hydration of the nucleus pulposus and its relation to intervertebral disc derangement.* J Bone Joint Surg Br, 1958. 40-B(1): p. 132-144.

[31] BROWN, T., HANSEN, R.J., and YORRA, A.J., *Some Mechanical Tests on the Lumbosacral Spine with Particular Reference to the Intervertebral Discs: A Preliminary Report.* J Bone Joint Surg Am, 1957. 39(5): p. 1135-1164.
[32] Bray, J. and Burbidge, H., *The canine intervertebral disk. Part Two: Degenerative changes--nonchondrodystrophoid versus chondrodystrophoid disks.* J Am Anim Hosp Assoc, 1998. 34(2): p. 135-144.
[33] Seiler, G., et al., *Staging of lumbar intervertebral disc degeneration in nonchondrodystrophic dogs using low-field magnetic resonance imaging.* Vet Radiol Ultrasound, 2003. 44(12718353): p. 179-184.
[34] Bartels, K.E., *Prophylactic laser disc ablation in dogs at Oklahoma State University.* Veterinary Medicine, 2007: p. 440-442.
[35] *Percutaneous Laser Disc Ablation (PLDA).* Available from: http://www.dfwvetsurgeons.com/t-plda.html.
[36] Wilson, B.C. and Jacques, S.L., *Optical reflectance and transmittance of tissues: principles and application.* IEEE Journal of Quantum Electronics, 1990. 26(12): p. 2186-2199.
[37] Delpy, D.T. and Cope, M., *Quantification in Tissue Near-Infrared Spectroscopy.* Philosophical Transactions: Biological Sciences, 1997. 352(1354): p. 649-659.
[38] Bensalah, K., et al., *Optical Reflectance Spectroscopy to Differentiate Benign From Malignant Renal Tumors at Surgery.* Urology, 2009. 73(1): p. 178-181.
[39] Prince, S. and Malarvizhi, S., *Monte Carlo simulation of NIR diffuse reflectance in the normal and diseased human breast tissues.* Biofactors, 2007. 30(18607075): p. 255-263.
[40] Nachabé, R., et al., *Effect of bile absorption coefficients on the estimation of liver tissue optical properties and related implications in discriminating healthy and tumorous samples.* Biomed. Opt. Express, 2011. 2(3): p. 600-614.
[41] Guenette, J.A., et al., *Blood flow index using near-infrared spectroscopy and indocyanine green as a minimally invasive tool to assess respiratory muscle blood flow in humans.* Am J Physiol Regul Integr Comp Physiol, 2011. 300(21289237): p. 984-992.
[42] Bender, J.E., et al., *Noninvasive monitoring of tissue hemoglobin using UV-VIS diffuse reflectance spectroscopy: a pilot study.* Opt. Express, 2009. 17(26): p. 23396-23409.
[43] Zonios, G., et al., *Diffuse Reflectance Spectroscopy of Human Adenomatous Colon Polyps In Vivo.* Appl. Opt., 1999. 38(31): p. 6628-6637.
[44] Friedland, S., et al., *Measurement of mucosal capillary hemoglobin oxygen saturation in the colon by reflectance spectrophotometry.* Gastrointest Endosc, 2003. 57(12665758): p. 492-497.
[45] Bhutani, V.K., et al., *Noninvasive measurement of total serum bilirubin in a multiracial predischarge newborn population to assess the risk of severe hyperbilirubinemia.* Pediatrics, 2000. 106(10920173).
[46] Schenkman, K.A. and Yan, S., *Propofol impairment of mitochondrial respiration in isolated perfused guinea pig hearts determined by reflectance spectroscopy.* Critical Care Medicine, 2000. 28(1): p. 172-177.

[47] Perelman, L.T., et al., *Observation of Periodic Fine Structure in Reflectance from Biological Tissue: A New Technique for Measuring Nuclear Size Distribution.* Physical Review Letters, 1998. 80(3): p. 627.
[48] Wang, X., et al., *Approximation of Mie scattering parameters in near-infrared tomography of normal breast tissue in vivo.* Journal of Biomedical Optics, 2005. 10(5): p. 051704-8.
[49] Fournell, A., et al., *Clinical evaluation of reflectance spectrophotometry for the measurement of gastric microvascular oxygen saturation in patients undergoing cardiopulmonary bypass.* Journal of Cardiothoracic and Vascular Anesthesia, 2002. 16(5): p. 576-581.
[50] Knoefel, W.T., et al., *Reflectance spectroscopy of pancreatic microcirculation.* J Appl Physiol, 1996. 80(8847291): p. 116-123.
[51] Sprigle, S., Linden, M., and Riordan, B., *Characterizing reactive hyperemia via tissue reflectance spectroscopy in response to an ischemic load across gender, age, skin pigmentation and diabetes.* Med Eng Phys, 2002. 24(12460724): p. 651-661.
[52] Harrison, G.I. and Young, A.R., *Ultraviolet radiation-induced erythema in human skin.* Methods, 2002. 28(1): p. 14-19.
[53] Ge, Z., Schomacker, K.T., and Nishioka, N.S., *Identification of Colonic Dysplasia and Neoplasia by Diffuse Reflectance Spectroscopy and Pattern Recognition Techniques.* Appl. Spectrosc., 1998. 52(6): p. 833-839.
[54] Georgakoudi, I., et al., *Fluorescence, Reflectance, and Light-Scattering Spectroscopy for Evaluating Dysplasia in Patients With Barrett's Esophagus.* Gastroenterology, 2001. 120(7): p. 1620-1629.
[55] Nordstrom, R.J., et al., *Identification of cervical intraepithelial neoplasia (CIN) using UV-excited fluorescence and diffuse-reflectance tissue spectroscopy.* Lasers in Surgery and Medicine, 2001. 29(2): p. 118-127.
[56] Mirabal, Y.N., et al., *Reflectance spectroscopy for in vivo detection of cervical precancer.* J Biomed Opt, 2002. 7(12421125): p. 587-594.
[57] Utzinger, U., et al., *Reflectance spectroscopy for in vivo characterization of ovarian tissue.* Lasers in Surgery and Medicine, 2001. 28(1): p. 56-66.
[58] Bigio, I.J., et al., *Diagnosis of breast cancer using elastic-scattering spectroscopy: preliminary clinical results.* J Biomed Opt, 2000. 5(10938787): p. 221-228.
[59] Breslin, T.M., et al., *Autofluorescence and diffuse reflectance properties of malignant and benign breast tissues.* Ann Surg Oncol, 2004. 11(14699036): p. 65-70.
[60] Lin, W.-C., et al., *In Vivo Brain Tumor Demarcation Using Optical Spectroscopy.* Photochemistry and Photobiology, 2001. 73(4): p. 396-402.
[61] Hoffmann, J., Lubbers, D.W., and Heise, H.M., *Applicability of the Kubelka-Munk theory for the evaluation of reflectance spectra demonstrated for haemoglobin-free perfused heart tissue.* Phys. Med. Biol. , 1998. 43(3571-3587).
[62] Müller, M.G., et al., *Spectroscopic detection and evaluation of morphologic and biochemical changes in early human oral carcinoma.* Cancer, 2003. 97(7): p. 1681-1692.

[63] Kollias, N. and Stamatas, G.N., *Optical non-invasive approaches to diagnosis of skin disease.* J. Invest. Dermatol. , 2002. 7: p. 64-75.
[64] Farrell, T.J., Patterson, M.S., and Wilson, B., *A diffusion theory model of spatially resolved, steady-state diffuse reflectance for the noninvasive determination of tissue optical properties in vivo.* Medical Physics, 1992. 19(4): p. 879-888.
[65] Zonios, G. and Dimou, A., *Modeling diffuse reflectance from semi-infinite turbid media: application to the study of skin optical properties.* Opt Express, 2006. 14(19529247): p. 8661-8674.
[66] Kim, A., et al., *A fiberoptic reflectance probe with multiple source-collector separations to increase the dynamic range of derived tissue optical absorption and scattering coefficients.* Opt. Express, 2010. 18(6): p. 5580-5594.
[67] Amelink, A. and Sterenborg, H.J.C.M., *Measurement of the Local Optical Properties of Turbid Media by Differential Path-Length Spectroscopy.* Appl. Opt., 2004. 43(15): p. 3048-3054.
[68] Kaspers, O.P., Sterenborg, H.J.C.M., and Amelink, A., *Controlling the optical path length in turbid media using differential path-length spectroscopy: fiber diameter dependence.* Appl. Opt., 2008. 47(3): p. 365-371.
[69] Johns, M., et al., *Determination of reduced scattering coefficient of biological tissue from a needle-like probe.* Opt. Express, 2005. 13(13): p. 4828-4842.
[70] Wang, L.V., *Biomedical Optics: Principles and Imaging*. 1st ed. 2007: Wiley-Interscience. 376.
[71] Weast, R.C. and Lide, D.R., *Handbook of Chemistry and Physics*. 67th ed. 1986: Chemical Rubber Company.
[72] Michels, R., Foschum, F., and Kienle, A., *Optical properties of fat emulsions.* Opt. Express, 2008. 16(8): p. 5907-5925.
[73] van Staveren, H.J., et al., *Light scattering in Intralipid-10% in the wavelength range of 400-1100 nm.* Appl. Opt., 1991. 30(31): p. 4507-4514.
[74] Pogue, B.W., et al., *Quantitative hemoglobin tomography with diffuse near-infrared spectroscopy: pilot results in the breast.* Radiology, 2001. 218(11152812): p. 261-266.
[75] Mourant, J.R., et al., *Predictions and measurements of scattering and absorption over broad wavelength ranges in tissue phantoms.* Appl Opt, 1997. 36(18250760): p. 949-957.
[76] Srinivasan, S., et al., *Interpreting hemoglobin and water concentration, oxygen saturation, and scattering measured in vivo by near-infrared breast tomography.* Proceedings of the National Academy of Sciences of the United States of America, 2003. 100(21): p. 12349-12354.
[77] Lentner, C., ed. *Geigy Scientific Tables* Vol. 3. 1984, Ciba-Geigy Ltd: Basel.
[78] Brunsting, A. and Mullaney, P.F., *Differential Light Scattering from Spherical Mammalian Cells.* Biophysical Journal, 1974. 14(6): p. 439-453.
[79] Weast, R.C. and Lide, D.R., *Handbook of Chemistry and Physics*. 65th ed. 1984: Chemical Rubber Company.
[80] Fujime, S., Takasaki-Ohsita, M., and Miyamoto, S., *Dynamic light scattering from polydisperse suspensions of large spheres.* Biophys J., 1988. 54(6): p. 1179-1184.

[81] Gobel, G., Kuhn, J., and Fricke, J., *Dependent scattering effects in latex-sphere suspensions and scattering powders.* Waves in Random Media, 1995. 5: p. 413-426.
[82] *Compact UV-VIS S2D2 fiber light source*. Available from: http://jp.hamamatsu.com/products/light-source/pd032/L10671/index_en.html.
[83] http://commons.wikimedia.org/wiki/File:Fluorescent_lighting_spectrum_peaks_labelled.gif.
[84] http://en.wikipedia.org/wiki/Intralipid.
[85] Stryer, L., *Biochemistry*. 1981, San Francisco: Freeman.

APPENDICES

A. External control of deuterium tungsten light source

Table A.1 External control terminals pinout of deuterium tungsten light source

PIN No.	Signal Name
1	S2D2 Lamp ON / OFF
2	Tungsten Lamp ON / OFF
3	Shutter Open / Close
4	S2D2 Lamp status signal
5	Tungsten lamp status signal
6	N.C.
7	Main power ON / OFF status signal
8	N.C.
9	N.C.
10	GND

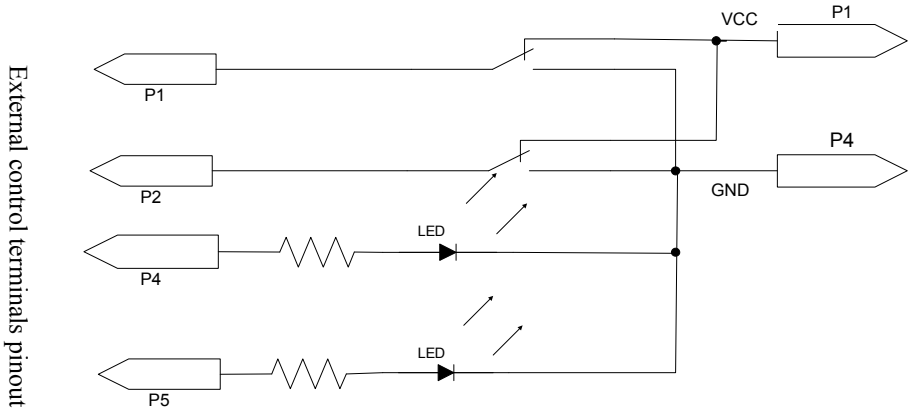

Fig. A.1 External control circuit of deuterium tungsten light source

B. Matlab Programs

```
% read spectrometer data.
% Input N is the number of data files
% Output Intensity is a 2012 by N matrix
% Output wavelength is a 2012 by 1 vector.

function [Intensity, Wavelength] =  readdata(N)
Intensity = zeros (2012,N);
for i = 1:N
   filename = 'data';
   k = num2str(i);
   fid = fopen ([filename k '.txt']);
   for n = 1:114
      A = fgetl(fid);
   end
   for n = 1:2012
      B = fgetl(fid);
      BN = str2num (B);
      Wavelength(n) = BN(2);
      Intensity (n,i) = BN (5);
   end
   fclose (fid);
end
end

% the spectrum analysis program
% spectrum calibration
% spectrum smooth
% powerlaw fits to calibrated spectrum
% Input wavelength (nm): the wavelength read from data file
% Input orignal_spectrum: the spectrum read from data file
% Input water_spectrum: the water spectrum read from data file used for calibration
% Input air_spectrum: the air spectrum read from data file used for calibration
% Output sc_spectrum: smoothed and calibrated spectrum
% Output a: fitted scattering amplitude
% Output b: fitted scattering power

function [sc_spectrum, a, b ] = spectrumanalysis (wavelength, orignal_spectrum, water_spectrum,
air_spectrum)

swl = wl(524:1665);
c_spectrum  =(original_spectrum-water_spectrum)./(air_spectrum-water_spectrum);
sc_spectrum = smooth ( c_spectrum(504:1685),100);
ft = fittype('power1');
cf=fit(swl'*1e-3, scpre_T8_9_1, ft);
a =  cf.a;
b =  cf.b;
end
```

```
% Mie scattering theory
% Input diameter (nm): the diameter vector of particles
% Input f: the size distribution vector
% Input N0: particle density
% Input n_s: scatter refractive index
% Input n_b: background refractive index
% Input lambda (nm): Interested wavelength range
% Output us_prime: reduced scattering coefficients (mm-1)
function [us_prime] = Mie (diameter, f, N0, n_s, n_b, lambda)

diameter = diameter*1e-9;
N = length (diameter);
radius = diameter/2;
lambda = lambda*1e-9;
M =length(lambda);
k = 2*pi*n_b/lambda;
n_rel = n_s/n_b;
err = 1e-8;
for m = 1:M
      Qs = zeros(N,1);
      gQs =zeros (N,1);
      for i = 1:N  % diameter
          x(i) = k(m)*radius(i);
          y(i) = n_rel(m)*x(i);
          for n = 1:10000
            Snx = sqrt(pi*x(i)/2)*besselj(n+0.5,x(i));
            Sny = sqrt(pi*y(i)/2)*besselj(n+0.5,y(i));
            Cnx = -sqrt(pi*x(i)/2)*bessely(n+0.5,x(i));
            Zetax = Snx+i*Cnx;

            Snx_prime = -(n/x(i))*Snx + sqrt(pi*x(i)/2)*besselj(n-0.5,x(i));
            Sny_prime = -(n/y(i))*Sny + sqrt(pi*y(i)/2)*besselj(n-0.5,y(i));
            Cnx_prime = -(n/x(i))*Cnx - sqrt(pi*x(i)/2)*bessely(n-0.5,x(i));
            Zetax_prime = Snx_prime+i*Cnx_prime;

            an_num = Sny_prime*Snx-n_rel*Sny*Snx_prime;
            an_den = Sny_prime*Zetax-n_rel*Sny*Zetax_prime;
            an = an_num/an_den;

            bn_num = n_rel*Sny_prime*Snx-Sny*Snx_prime;
            bn_den = n_rel*Sny_prime*Zetax-Sny*Zetax_prime;
            bn = bn_num/bn_den;

            Qs1 = (2*n+1)*(abs(an)^2+abs(bn)^2);
            Qs(i) = Qs(i) + Qs1;

            if n>1
               gQs1 = (n-1)*(n+1)/n*real(an_1*conj(an)+bn_1*conj(bn))+
                           (2*n-1)/((n-1)*n)*real(an_1*conj(bn_1));
               gQs(i) = gQs(i)+gQs1;
            end
```

```
            an_1 = an;
            bn_1 = bn;

            if (abs(Qs1)<(err*Qs(i)) & abs(gQs1)< (err*gQs(i)))
               break;
            end
          end
        end
        Qs = (2./x.^2)'.* Qs;
        gQs = (4./x.^2)'.*gQs;
        g = gQs./Qs;
        qs  = pi*radius'.^2.*Qs;

        mus(m) = N0*sum ((qs.*f'))*1e-3;
        ga(m) = sum (g.*qs.*f')./sum (qs.*f');
        mus_prime(m) = mus(m).*(1-ga(m));
end
end
```

VITA

Yuanyuan Jiang

Candidate for the Degree of

Master of Science

Thesis: FEASIBILITY OF MINIMALLY INVASIVE FIBER BASED EVALUATION OF CHONDRODYSTROPHOID CANINE INTERVERTEBRAL DISC BY REFLECTANCE SPECTROSCOPY

Major Field: Electrical and Computer Engineering

Biographical:

Education:

Master of Science in Electrical and Computer Engineering in Oklahoma State University, Stillwater, Oklahoma, May, 2011.

Master of Science in Precision Instrument and Opto-Electronics Engineering in Tianjin University, Tianjin, China, 2008.

Bachelor of Science in Precision Instrument and Opto-Electronics Engineering in Tianjin University, Tianjin, China, 2006.

Name: Yuanyuan Jiang Date of Degree: May, 2011

Institution: Oklahoma State University Location: Stillwater, Oklahoma

Title of Study: FEASIBILITY OF MINIMALLY INVASIVE FIBER BASED EVALUATION OF CHONDRODYSTROPHOID CANINE INTERVERTEBRAL DISC BY REFLECTANCE SPECTROSCOPY

Pages in Study: 84 Candidate for the Degree of Master of Science

Major Field: Electrical and Computer Engineering

Scope and Method of Study:

The objective of this study is to investigate the feasibility of using a fiber-needle spectroscopy sensor to analyze the changes of tissue compositions involved in the chondrodystrophoid condition of the canine intervertebral disc.

Findings and Conclusions:

Reflectance spectrum of single fiber reflectance spectroscopy is expected to provide information of scattering and absorption compositions of tissue in proximity to the fiber-tip. The reflectance spectrum model of single fiber reflectance spectroscopy has been validated by Intralipid and polystyrene phantoms studies. Preliminary measurements on cadaveric canine intervertebral discs indicated significant reduction of scattering constituents and possible diminishment of water content after percutaneous laser disc ablation (PLDA). Cadaveric measurements revealed that the calcified discs have higher scattering amplitude and lower scattering power than normal discs. And when using scattering amplitude to differentiate the normal and calcified discs, 99.28% area under curve has been achieved according to Receiving Operating Characteristic (ROC) curve. Although the water content could not be quantitatively calculated, the absorption from water is observed in the reflectance spectrum. Intralipid phantom study and cadaveric measurements reveal that fiber-needle based sensing configuration may be feasible for integrating the evaluation of calcification and water content into the work-flow of Ho:YAG laser disc ablation for pre-operative in-line detection and post-operative evaluation of therapeutic interventions regarding the chondrodystrophic disc.

ADVISER'S APPROVAL Dr. Daqing Piao